



HAL
open science

Downscaling of solar-induced chlorophyll fluorescence from canopy level to photosystem level using a random forest model

Xinjie Liu, Luis Guanter, Liangyun Liu, Alexander Damm, Zbyněk Malenovský, Uwe Rascher, Dailiang Peng, Shanshan Du, Jean-Philippe Gastellu-Etchegorry

► To cite this version:

Xinjie Liu, Luis Guanter, Liangyun Liu, Alexander Damm, Zbyněk Malenovský, et al.. Downscaling of solar-induced chlorophyll fluorescence from canopy level to photosystem level using a random forest model. *Remote Sensing of Environment*, 2019, 231, pp.110772. 10.1016/j.rse.2018.05.035 . hal-04644171

HAL Id: hal-04644171

<https://hal.science/hal-04644171v1>

Submitted on 4 Sep 2024

HAL is a multi-disciplinary open access archive for the deposit and dissemination of scientific research documents, whether they are published or not. The documents may come from teaching and research institutions in France or abroad, or from public or private research centers.

L'archive ouverte pluridisciplinaire **HAL**, est destinée au dépôt et à la diffusion de documents scientifiques de niveau recherche, publiés ou non, émanant des établissements d'enseignement et de recherche français ou étrangers, des laboratoires publics ou privés.

1 **Downscaling of solar-induced chlorophyll fluorescence from** 2 **canopy level to photosystem level using a random forest** 3 **model**

4
5 Xinjie Liu^{a,b}, Luis Guanter^b, Liangyun Liu^{a,*}, Alexander Damm^{c,d}, Zbyněk Malenovský^{e,f},
6 Uwe Rascher^g, Dailiang Peng^a, Shanshan Du^a, Jean-Philippe Gastellu-Etchegorry^h

7
8 ^a Key Laboratory of Digital Earth Science, Institute of Remote Sensing and Digital Earth, Chinese Academy
9 of Sciences, Beijing 100094, China

10 ^b Helmholtz Center Potsdam, GFZ German Research Center for Geosciences, Remote Sensing Section,
11 Telegrafenberg A17, 14473 Potsdam, Germany

12 ^c Remote Sensing Laboratories, Department of Geography, University of Zurich, Winterthurerstrasse 190,
13 8057 Zurich, Switzerland

14 ^d Department of Surface Waters – Research and Management, Eawag, Swiss Federal Institute of Aquatic
15 Science and Technology, 8600 Dübendorf, Switzerland

16 ^e Surveying and Spatial Sciences, School of Technology Engineering and Design, University of Tasmania,
17 Private Bag 76, TAS 7001 Hobart, Australia

18 ^f Centre for Sustainable Ecosystem Solutions, School of Biological Sciences, University of Wollongong, NSW
19 2522 Wollongong, Australia

20 ^g Institute of Bio- and Geosciences, IBG-2: Plant Sciences, Forschungszentrum Jülich, Leo-Brandt-Str.,
21 52425 Jülich, Germany

22 ^h Toulouse University - CESBIO (CNRS, CNES, IRD, Paul Sabatier University), Toulouse, France

23

24 **Abstract**

25 Solar-induced chlorophyll fluorescence (SIF), an electromagnetic signal that can potentially indicate
26 vegetation photosynthetic activity, can be retrieved from ground-based, airborne and satellite
27 measurements. However, due to the scattering and re-absorption effects inside the leaves and canopy,
28 SIF measured at the canopy level is only a small part of the total SIF emission at the photosystem

* Corresponding author. Email: liuly@radi.ac.cn; Address: No.9 Dengzhuang South Rd., Haidian, Beijing, 100094, China.

29 level. Therefore, a downscaling mechanism of SIF from the canopy level to the photosystem level is
30 important for better understanding the relationship between SIF and the vegetation gross primary
31 production (GPP). In this study, firstly, we analyzed the canopy scattering effects using a simple
32 parameterization model based on the spectral invariant theory. The probability for SIF photons to
33 escape from the canopy was found to be related to the anisotropic spectral reflectance, canopy
34 interception of the upward solar radiation, and leaf absorption. An empirical approach based on a
35 Random Forest (RF) regression algorithm was applied to downscale SIF constrained by the red,
36 red-edge and far-red anisotropic reflectance. The RF was trained using simulations conducted with
37 the Soil Canopy Observation, Photochemistry and Energy fluxes (SCOPE) model. The performance of
38 the SIF downscaling method was evaluated with SCOPE and Discrete Anisotropic Radiative Transfer
39 (DART) model simulations, ground measurements and airborne data. Results show that estimated
40 SIF at the photosystem level matches well with simulated reference data, and the relationship
41 between SIF and photosynthetically active radiation absorbed by chlorophyll is improved by SIF
42 downscaling. This finding in combination with other evaluation criteria suggests the downscaling of
43 canopy SIF as an efficient strategy to normalize species dependent effects of canopy structure and
44 varying solar-view geometries. Based on our results for the SIF-APAR relationship, we expect that
45 such normalization approaches can be helpful to improve estimates of photosynthesis using remote
46 sensing measurements of SIF.

47 **Keywords:** Solar-induced chlorophyll fluorescence; Downscaling; Canopy level; Photosystem level;
48 Spectral invariant theory; Random Forest regression

49 1. Introduction

50 Solar-induced chlorophyll fluorescence (SIF) has been proved to be an efficient tool for
51 monitoring of gross primary production (GPP), showing large advantages compared with other
52 remote sensing indicators based on reflectance-data (Guanter et al. 2014; Migliavacca et al. 2017;
53 Porcar-Castell et al. 2014; Sun et al. 2017; Zhang et al. 2016). The photosynthetically active energy
54 absorbed by leaf pigments can be: i) used in photochemical reactions, ii) dissipated as heat, or iii)
55 re-emitted as fluorescence (Porcar-Castell et al. 2014). Unlike the reflectance based parameters, SIF is,
56 as a by-product of photosynthesis, more directly related to GPP (Berry et al. 2012; Coops et al. 2010;
57 Damm et al. 2015a; Zarco-Tejada et al. 2013).

58 Validity of the resource balancing paradigm (Field et al. 1998) in combination with the Monteith
59 light use efficiency (LUE) model (Monteith 1972; Monteith and Moss 1977) is the foundation of most
60 of the approaches for the estimation of GPP from remote sensing data. The LUE model can be
61 expressed as:

$$62 \quad \text{GPP} = \text{PAR} \times \text{fAPAR} \times \text{LUE} \quad (1)$$

63 where PAR stands for the photosynthetically active radiation, fAPAR is the fraction of PAR absorbed
64 by vegetation, and LUE is the light use efficiency, defined as the number of μmol of CO_2 absorbed per
65 μmol of photons.

66 Similarly, the total SIF emission at the photosystem (PS) level (the total SIF emission inside the
67 leaves without any scattering or re-absorption) can be expressed as (Berry et al. 2012; Liu et al.
68 2017a; Moya and Cerovic 2004; Porcar-Castell et al. 2014; Wieneke et al. 2016):

$$69 \quad \text{SIF}_{\text{PS}}(\lambda) = \text{PAR} \times \text{fAPAR} \times F_{\text{yield}}(\lambda) \quad (2)$$

70 where λ is the wavelength, and F_{yield} is the quantum yield for chlorophyll fluorescence. If F_{yield} is
71 constant, then SIF_{PS} is linearly related to the PAR absorbed by vegetation.

72 In recent years, we have been experiencing a rapid development of methods for SIF retrieval
73 from spectral remote sensing data (Malenovský et al. 2009). The SIF signal can be detected by
74 ground-based (Grossmann 2014; Liu et al. 2017a; Liu et al. 2015; Liu et al. 2005; Wyber et al. 2017;
75 Yang et al. 2015; Cogliati et al. 2015; Burkart et al. 2015), airborne (Damm et al. 2014, Rascher et al.
76 2015; Wieneke et al. 2016), and space-borne sensors (Frankenberg et al. 2011; Guanter et al. 2012;
77 Joiner et al. 2013; Joiner et al. 2011; Köhler et al. 2015). However, SIF is emitted by chlorophyll *a*
78 molecules, which are contained inside chloroplasts at different leaf mesophyll layers. Reabsorption
79 and scattering of SIF are both taking place inside leaves as well as within the canopy. Using remote
80 sensing approaches at large scales, it is only possible to measure SIF at the canopy level ($\text{SIF}_{\text{Canopy}}$,
81 defined as SIF escaping from the canopy in a specific viewing direction).

82 The SIF spectrum extends over the wavelength range from about 640 to 850 nm, with two peaks
83 centered at 685 nm and 740 nm. Ramos and Lagorio (2004) pointed out that the spectral shape of
84 fluorescence measured at leaf level was influenced by the leaf re-absorption, and developed a model
85 to correct the spectral shape using leaf reflectance. Van Wittenberghe et al. (2015) studied the
86 upward and downward SIF emission at the leaf level separately using a special leaf probe called
87 FluoWat, and found that the partitioning of the upward and downward SIF components is influenced
88 by scattering and absorption processes related to the leaf structure and the pigment content. This
89 indicates that the red SIF at 685 nm is strongly influenced by chlorophyll absorption within the leaves,
90 while far-red SIF is mainly influenced by scattering effect of leaf tissue structures. Several studies
91 have reported a decrease in the red/far-red SIF ratio from leaf level to canopy level (Fournier et al.

92 2012; Moya et al. 2006; Romero et al. 2018), which can be, besides the environmental stress exposure
93 (Ač et al. 2015), explained by the strong re-absorption of SIF by chlorophyll at the red band
94 (Daumard et al. 2012; Fournier et al. 2012; Agati et al. 1993; Cordon et al. 2006; Porcar-Castell et al.
95 2014; Romero et al. 2018). Liu et al. (2016) observed similar anisotropic characteristics for SIF and
96 reflectance at the canopy level, and claimed that the phenomenon can be attributed to re-absorption
97 by canopy components and the bidirectional canopy gap fraction. Other studies also reported a
98 similar anisotropic effect for SIF retrieved from space (e.g. Guanter et al. 2012, Joiner et al. 2012),
99 while He et al. (2017) proved that an angular normalization of SIF strengthens SIF-GPP relationships.
100 Further, Du et al. (2017) reported a species-dependent relationship between SIF_{canopy} and PAR
101 absorbed by chlorophyll ($APAR_{\text{chl}}$), and pointed out that the uncertainty in the SIF escape probability
102 weakens the relationship between SIF and $APAR_{\text{chl}}$ or GPP, especially at the red band. Therefore,
103 downscaling of SIF from canopy level to PS level is important to better constrain estimates of GPP
104 using remote sensing observations of SIF.

105 There are two very recent studies focusing on the problem of SIF downscaling. Romero et al.
106 (2018) developed a physical model based on the canopy reflectance, canopy transmittance and soil
107 reflectance to correct the spectral shape of fluorescence emission from canopy level to leaf level.
108 Together with the study by Ramos and Lagorio (2004), the fluorescence spectral shape at PS level
109 could also be retrieved. However, the absolute SIF intensity was not available. Yang and Van der Tol
110 (2018) linked the canopy scattering of far-red SIF to the canopy reflectance, canopy interceptance
111 and leaf albedo based on canopy radiative transfer analysis, but the model was not valid for the red
112 band and the input parameters were not easy to be accurately measured or estimated. Moreover, the
113 SIF downscaling from leaf level to PS level was not included.

114 Given the fact that the radiative transfer of emitted SIF within a canopy is similar to that for
115 scattered solar radiation, it can be assumed that the modelling of top-of-canopy (TOC) spectral
116 reflectance can approximate the canopy effects on SIF, which is needed for the estimation of SIF
117 escape probability from PS level to canopy level (ϵ_{CP}) (Van der Tol et al. 2009; Liu et al. 2016). To
118 express the radiative transfer equation within the canopy together with the leaf scattering coefficient,
119 Knyazikhin et al. (1998) introduced a spectral invariant p , which was defined by Smolander and
120 Stenberg (2005) as photon recollision probability. Another spectral invariant, bi-directional gap
121 fraction, was introduced to quantify the probability of scattered photons to escape the canopy via
122 gaps in the direction of viewing (Huang et al. 2007; Knyazikhin et al. 2011). The so-called ‘spectral
123 invariant theory’ has been successfully used to better understand the absorption and scattering
124 effects within the canopy and also to link the reflectance at the canopy level and leaf level (Huang et
125 al. 2007; Knyazikhin et al. 2013; Smolander and Stenberg 2005; Stenberg et al. 2016; Wang et al.
126 2003). Similarly, the spectral invariant theory can be applied to model the escape probability for SIF
127 with a number of parameters describing the leaf optical properties, canopy structure, and
128 background reflectance. However, these parameters are usually difficult to accurately measure or
129 estimate. Moreover, spectral invariant theory can only model the radiative transfer process from leaf
130 level to canopy level, while SIF is emitted from inside the leaves, which means that the re-absorption
131 of SIF photons within the leaves (leaf internal absorption) is not accounted for. Although the canopy
132 reflectance also contains information about the leaf absorption, it is difficult to directly link this to the
133 SIF absorption inside the leaves.

134 Supervised machine learning approaches trained on appropriate training dataset are capable of
135 building accurate prediction models (Ma, 2014) that can empirically overcome the difficulties in the

136 physical modelling described above (the unavailable input parameters for the physical model can be
137 estimated by machine learning approaches using available information). The physically based
138 analysis of the radiative transfer process is, in turn, able to point out the appropriate input
139 parameters used in the machine learning methods.

140 This study aims to define and evaluate a practical solution for the downscaling of SIF from the
141 canopy level to the PS level. The SIF radiative transfer within canopy and inside leaves is analyzed
142 based on the spectral invariant theory and leaf-level simulations to define the key parameters driving
143 the SIF downscaling from canopy level to leaf and PS levels. We then employ an empirical approach
144 based on random forest (RF) regression (Breiman 2001) to predict the SIF escape probability from
145 leaf level to canopy level (ϵ_{CL}) and from PS level to canopy level (ϵ_{CP}) using reflectance information.
146 The Soil Canopy Observation, Photochemistry and Energy fluxes (SCOPE) model (Van der Tol et al.
147 2009) was then used for the simulation of the training dataset. Finally, we evaluate the performance
148 of the SIF downscaling using SCOPE and Discrete Anisotropic Radiative Transfer (DART) model
149 simulations, ground and airborne data. The presented approach facilitates the normalization of SIF
150 observations across canopy types observed under varying sun-view geometries, and eventually
151 improves our understanding on the relationship between SIF emission and photosynthetic activity.

152 **2. Materials and methods**

153 **2.1 Simulated datasets**

154 **2.1.1 SCOPE simulation**

155 The SCOPE model (Van der Tol et al. 2009) is a vertical (1-D) integrated radiative transfer and

156 energy balance model, which is able to simulate leaf and canopy spectral reflectance and SIF as well
 157 as photosynthesis and water and heat flux by linking the radiative transfer with micro-meteorological
 158 processes. SCOPE has been widely used in the field of SIF research (e.g. Verrelst et al. 2015; Zhang et
 159 al. 2016; Yang and Van der Tol. 2018). The latest version of SCOPE (v1.7) provides users with SIF at
 160 canopy level, leaf level (SIF emitted by all leaves, excluding the re-absorption and scattering within
 161 the canopy) and at PS level (SIF emitted by all photosystems, excluding the re-absorption within the
 162 leaves). Therefore, we used SCOPE v1.7 for the simulation of SIF at the canopy, leaf and PS levels,
 163 along with that of the canopy directional reflectance, leaf reflectance and transmittance.

164 In the SIF emission spectral range ($\sim 640 - 850$ nm), the amount of absorption by leaves is
 165 mainly related to chlorophyll content (Jacquemoud and Baret 1990). The canopy scattering is mainly
 166 related to the canopy structure parameters (leaf area index (LAI), leaf inclination distribution, etc.)
 167 and solar-view geometries (solar zenith angle (SZA), view zenith angle (VZA) and relative azimuth
 168 angle (RAA)) (Verhoef 1984). We parameterized SCOPE for sets of different leaf chlorophyll contents
 169 (C_{ab}), LAI levels and six typical leaf inclination distributions to cover most common vegetation
 170 conditions. Additionally, different SZAs and VZAs in the solar principal plane were also defined. The
 171 full-width-at-half-maximum spectral response (FWHM) and spectral sampling interval (SSI) for the
 172 SCOPE simulations are 1 nm. Details about the SCOPE input parameters are listed in Table 1. As a
 173 result, 6240 different samples were generated.

174 Table 1. Main input parameters for the SCOPE simulations.

Parameter	Values	Unit	Description
C_{ab}	20, 40, 60, 80	$\mu\text{g}/\text{cm}^2$	Leaf chlorophyll a + b content
C_{dm}	0.012	g/cm^2	Dry matter content
C_w	0.009	cm	Leaf water equivalent layer
N	1.4	-	Leaf mesophyll scattering parameter
LAI	1, 2, 3, 4	m^2/m^2	Leaf area index
$LIDF_a$	1, -1, 0, 0, -0.35, 0	-	Leaf inclination parameter

LIDF _b	0, 0, -1, 1, -0.15, 0	-	Bimodality parameter
FQE	0.01	-	Fluorescence quantum yield efficiency
SZA	20, 30, 40, 50, 60	degree	Solar zenith angle
VZA	0, 10, 20, 30, 40, 50, 60	degree	View zenith angle
RAA	0, 180	degree	Relative azimuth angle

175 2.1.2 DART simulation

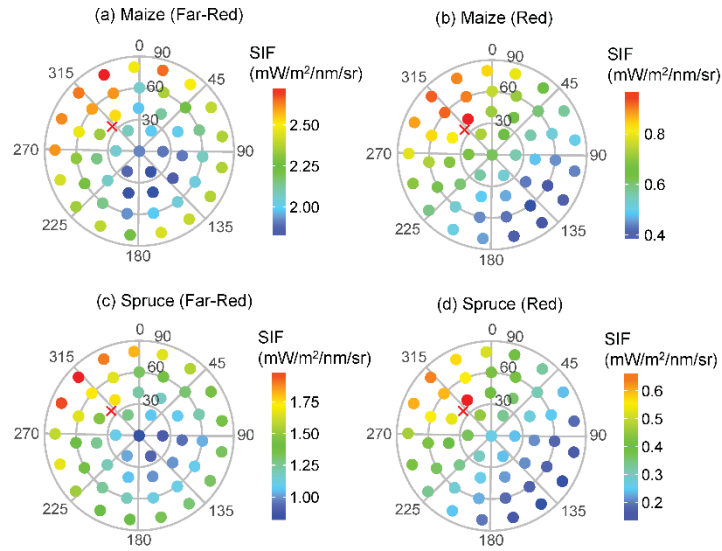
176 DART is a three-dimensional (3-D) radiative transfer model that allows simulating the radiation
177 budget as well as remotely sensed images of natural and urban surfaces covering the range from the
178 ultraviolet to the thermal infrared band (Gastellu-Etcheberry et al. 2015). Recently, a SIF module that
179 allows simulations of SIF radiative transfer within 3-D canopies has been added to DART
180 (Gastellu-Etcheberry et al. 2017). Similar to SCOPE, DART uses the Fluspect model (Vilfan et al. 2016)
181 to simulate the reflectance, transmittance and SIF emission at the leaf level. In this study, the DART
182 model (v5.6.6) was employed to simulate SIF at both the canopy and leaf levels, together with the
183 directional reflectance of 50 different viewing angles for two geometrically explicit and
184 architecturally different canopies of maize (*Zea mays L.*) and Norway spruce (*Picea abies /L./ H.*
185 *Karst.*). The DART parameterization details are listed in Table 2. Figure 1 shows the simulated
186 multi-angular SIF at canopy level for maize and spruce at the far-red (740 nm) and red bands (687
187 nm).

188 Table 2. Major input parameters for the DART simulations of maize and spruce canopies.

Parameter	Values	Unit	Description
C_{ab}	58	$\mu\text{g}/\text{cm}^2$	Leaf chlorophyll a + b content
C_{dm}	0.0037	g/cm^2	Dry matter content
C_w	0.0131	cm	Leaf water equivalent layer
N	1.518	-	Leaf mesophyll scattering parameter
LAI	4 (maize), 7 (spruce)	m^2/m^2	Leaf area index
Canopy Height	2.25 (maize), 10 (spruce)	m	Canopy Height
FQE (PSI)	0.002	-	Fluorescence quantum yield efficiency for photosystem I
FQE (PSII)	0.008	-	Fluorescence quantum yield

			efficiency for photosystem II
SZA	37.94	degree	Solar zenith angle
VZA	15 – 65	degree	View zenith angle
SAA	311.89	degree	Solar azimuth angle
VAA	0 – 180	degree	View azimuth angle

189



190

191 Figure 1. Multi-angular SIF at canopy level for maize and spruce at the far-red (740 nm) and red (687

192 nm) bands, as simulated by DART. The labels are the view azimuth ($0^\circ - 360^\circ$, 0° for the north) and

193 zenith ($0^\circ - 90^\circ$) angles. The red cross indicates the solar position (zenith angle: 37.94° ; azimuth

194 angle: 311.89°). The incident PAR is 1185.76 W/m^2 , and the temperature is 300 K.

195

196 2.2 Ground measurements

197 2.2.1 Multi-species experiments

198 A dataset comprising ground spectral measurements of different species, acquired at three sites,

199 following three specific experimental settings was used to evaluate the performance of SIF

200 downscaling for different canopy structures.

201 Spectral measurements of winter wheat (*Triticum*) were carried out on five days at the National
202 Precision Agriculture Demonstration Base located at Xiao Tangshan Farm (XTS, 40°11'N, 116°27'E),
203 north of Beijing, China. Diurnal cycles of radiance measurements (nadir view) were conducted on
204 April 8 - 9 and 18, 2016, when the growth stages of the winter wheat were jointing and booting, and
205 on November 7 and December 8, 2016 when the growth stages were emergence and tillering,
206 respectively. The leaf inclination distribution function (LIDF) of winter wheat was assumed to be
207 spherical based on a visual inspection.

208 Measurements of cotton (*Gossypium*) and different kinds of vegetables (i.e. sweet potato
209 (*Ipomoea batatas*), Chinese cabbage (*Brassica rapa pekinensis*), thyme (*Thymus*), pumpkin (*Cucurbita*
210 *Cucurbita*)) were carried out on December 18, 2016 at Nanbin Farm (NBF, 18°22'N, 109°10'E) in
211 Hainan Province, China. The LIDF types of the vegetables and cotton are mostly close to planophile
212 based on visual assessment. For convenience, the term 'vegetables' is used to represent all the species
213 on this site (including cotton).

214 Diurnal measurements of gold coin grass (*Lysimachiae Herba*) were also carried out on
215 December 18, 2016 at the Sanya Remote Sensing Satellite Data Receiving Station (SYS, 18°18'N,
216 109°18'E) in Hainan Province, China. The LIDF of this grass was assessed to be close to planophile by
217 visual inspection.

218 Details of the multi-species measurements described above are summarized in Table 3. All the
219 spectral measurements were conducted using a customized Ocean Optics QE Pro spectrometer
220 (Ocean Optics, Dunedin, FL, USA), characterized by a FWHM of 0.31 nm, a SSI of 0.155 nm, and a peak
221 signal-to-noise ratio (SNR) higher than 1000. For more details of the experiments, please refer to [Du](#)
222 [et al. \(2017\)](#).

223 Table 3. Parameters of multi-species measurements. Cab stands for leaf chlorophyll a+b content, LIDF
 224 is the leaf inclination distribution function, and Fc is the fraction of vegetation coverage.

Site	Location	Date	Species	Cab ($\mu\text{g}/\text{cm}^2$)	LIDF	Fc
Xiao Tangshan (XTS)	40°11'N 116°27'E	Apr. 8, 9 & 18, Nov. 7, Dec. 8, 2016	Winter wheat	21.22 – 55.29	Spherical	0.15 – 0.79
Nanbin Farm (NBF)	18°22'N 109°10'E	Dec. 18, 2016	Vegetables and cotton	15.22 – 56.68	Planophile	0.28 – 0.91
Sanya Station (SYS)	18°18'N 109°18'E	Dec. 18, 2016	Gold coin grass	40.83	Planophile	0.67

225

226 2.2.2 Multi-angular experiments

227 Due to the influence of the canopy structure (i.e. variable gap fraction and LIDF), SIF at the
 228 canopy level is anisotropic. To test the performance of the SIF downscaling algorithm, we carried out
 229 a series of multi-angular measurements on a winter wheat canopy during the springs of 2015 and
 230 2016 at the Xiao Tangshan Farm, Beijing, China, using a multi-angular observation system (MAOS)
 231 (Yan et al. 2012). The MAOS consists of a two-dimensional automatic goniometer, a spectrometer (QE
 232 Pro) and a laptop for control. It automatically collects the canopy radiance at different viewing angles,
 233 together with the downwelling solar irradiance reflected from a reference panel. In this study, the
 234 multi-angular spectral measurements were taken in the solar principal planes with the view zenith
 235 angles ranging from -60° to 60° with an interval of 10° (a smaller interval of 2° was set around the
 236 hotspot position). The multi-angular measurements of canopy reflectance and SIF were carried out
 237 under stable sunny weather conditions from 8:00 to 16:30 (local time) during eight days of different
 238 winter wheat growth stages in 2015 and 2016 (as listed in Table 4). It takes about 7 minutes for each
 239 set of multi-angular measurements. In total, 32 sets of valid measurements were acquired.

240 Table 4. Parameters of multi-angular measurements on winter wheat at Xiao Tangshan Farm, Beijing,
 241 China during the springs of 2015 and 2016.

Date	LAI	Cab ($\mu\text{g}/\text{cm}^2$)	SZA ($^\circ$)
Apr. 3, 2015	1.46	47.9	43.6 – 54.5
Apr. 13, 2015	1.94	51.5	38.4 – 57.8
Apr. 24, 2015	2.40	50.0	32.3 – 47.4
Apr. 25, 2015	2.40	50.0	31.1 – 62.4
Apr. 18, 2016	2.92	47.5	36.4 – 61.5
May 3, 2016	1.93	49.3	29.3 – 50.5
May 4, 2016	1.93	49.3	32.8 – 60.5
May 17, 2016	1.43	45.6	27.4 – 47.6

242 2.2.3 SIF retrieval

243 At the canopy level, measured radiance signals comprise the sum of emitted SIF and reflected solar
 244 radiation. Disentangling both components is frequently based on the Fraunhofer Line Discrimination
 245 (FLD) principle (Plascyk 1975). Frequently used algorithms include the 3-band FLD (3FLD) (Maier et
 246 al. 2003), the improved FLD (iFLD) (Alonso et al. 2008) and the spectral fitting methods (SFM)
 247 (Meroni et al. 2010). According to the analysis by Damm et al (2011) and Liu et al. (2015), the 3FLD
 248 algorithm is relatively simple and robust for the spectral resolution and SNR of the spectral data
 249 acquired by our QE Pro spectrometer. Therefore, we estimated SIF at the canopy level with the 3FLD
 250 algorithm. The selected wavelengths are 757.92 nm, 760.72 nm and 768.87 nm for the O2-A band,
 251 and 686.44 nm, 687.09 nm and 688.23 nm for O2-B band (Du et al. 2017).

252 2.2.4 Estimation of APAR_{chl}

253 According to Eq. (2), SIF emission at photosystem level is closely related to APAR (more
 254 specifically, PAR absorbed by chlorophyll (APAR_{chl})). APAR_{chl} is difficult to measure directly, but is
 255 closely related to the photosynthetically active radiation absorbed by green leaves (APAR_{green}) (Du et

256 al. 2017; Porcar-Castell et al. 2014). Liu et al. (2013) proposed an efficient method for making *in-situ*
 257 measurements of the fraction of $APAR_{green}$ ($fAPAR_{green}$) for a low vegetation canopy using a digital
 258 camera and a reference panel. A color image of the canopy with the reference panel is first taken by a
 259 digital camera at nadir position. Pixels in the image are then classified into green leaves, ground litter,
 260 sunlit soil, shaded soil, and reference panel. Consequently, the $fAPAR_{green}$ could be calculated as:

$$261 \quad fAPAR_{green} = \frac{PAR_i - PAR_r - (APAR_{EB} + APAR_{CB})}{PAR_i} \quad (3)$$

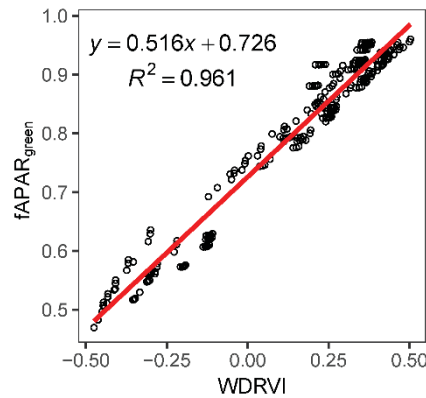
262 where PAR_i and PAR_r are, respectively, the incident and reflected (including all exposed components)
 263 PAR derived from the DN values of the digital image. $APAR_{EB}$ and $APAR_{CB}$ are the PAR absorbed by the
 264 exposed background (EB, including the non-photosynthetic components) and the vegetation-covered
 265 background (CB) respectively.

266 In the multi-species experiments described in Section 2.2.1, $fAPAR_{green}$ was measured with the
 267 digital camera based approach as described above. Unfortunately, $fAPAR_{green}$ was not measured in the
 268 multi-angular experiments (Section 2.2.2). To eliminate the saturation effect of the normalized
 269 difference vegetation index (NDVI), Gitelson (2004) proposed a wide dynamic range vegetation index
 270 (WDRVI), which has been proved to be well linearly correlated with $fAPAR_{green}$ (Viña and Gitelson
 271 2005). The WDRVI is defined as:

$$272 \quad WDRVI = (\alpha R_{NIR} - R_{Red}) / (\alpha R_{NIR} + R_{Red}) \quad (4)$$

273 where R_{NIR} and R_{Red} are the reflectances at the near infrared and red band, respectively, and α is a
 274 weighting coefficient with a value of 0.1 – 0.2 (Gitelson 2004). Figure 2 shows the relationship
 275 between WDRVI ($\alpha = 0.1$) and $fAPAR_{green}$ for SCOPE simulations with different values of the LAI (1 –
 276 4), leaf chlorophyll content (20 – 80 $\mu\text{g}/\text{cm}^2$), SZA (20 – 60 °) and three typical leaf inclination
 277 distribution functions (planophile, plagiophile and spherical). Therefore, in the multi-angular

278 experiments $fAPAR_{green}$ was estimated using the linear model based on the WDRVI.



279

280 Figure 2. Linear regression of the fraction of photosynthetically active radiation absorbed by green

281 leaves ($fAPAR_{green}$) on the wide dynamic range vegetation index (WDRVI) computed from SCOPE

282 simulations for canopies with different leaf area indices, leaf chlorophyll contents and leaf inclination

283 distributions.

284 Chlorophyll is the main absorbing compound for PAR in green leaves (Jacquemoud and Baret

285 1990; Porcar-Castell et al. 2014). According to Du et al. (2017), $fAPAR_{chl}$ can be approximated from

286 $fAPAR_{green}$ with a linear function:

$$287 \quad fAPAR_{chl} = k \times fAPAR_{green} \quad (5)$$

288 where the coefficient k is related to the leaf chlorophyll content. Analysis of SCOPE simulations

289 conducted by Du et al. (2017) revealed that the value of k varies from 0.78 to 0.80 for the leaf

290 chlorophyll content from 20 to 60 $\mu\text{g}/\text{cm}^2$. Since the leaf chlorophyll content of most of the samples

291 was within the range 20 – 60 $\mu\text{g}/\text{cm}^2$ (except for one sample for which the value was 15.22 $\mu\text{g}/\text{cm}^2$),

292 we estimated $fAPAR_{chl}$ using k equal to 0.79 in this study.

293 The incident photosynthetically active radiation (PAR) was calculated using the radiance

294 reflected from a white reference panel measured by a spectrometer. Consequently, the $APAR_{chl}$ can be

295 calculated as:

296
$$\text{APAR}_{\text{chl}} = \text{PAR} \times f\text{APAR}_{\text{chl}} \quad (6)$$

297 **2.3 Airborne measurements**

298 The airborne image, used to evaluate the method introduced in this study, was acquired using
299 the imaging spectrometer *HyPlant* (Specim, Oulo, Finland). As an airborne demonstrator for the ESA's
300 Fluorescence Explorer (FLEX) mission, *HyPlant* was specifically designed for the monitoring of
301 vegetation canopy spectral characteristic parameters, including SIF. There are two modules in
302 *HyPlant*: the first is the FLUO module, which is used for the SIF measurements and which covers the
303 range from 670 nm to 780 nm with a high spectral resolution (FWHM = 0.25 nm); the other module is
304 the DUAL module, which covers a broader spectral range (380 – 2500 nm) with a FWHM of ~ 4 nm
305 for bands from 380 nm to 970 nm, and of ~ 13.3 nm for bands from 970 nm to 2500 nm. More
306 technical details about the *HyPlant* configurations and the data processing are available in [Rascher et](#)
307 [al. \(2015\)](#).

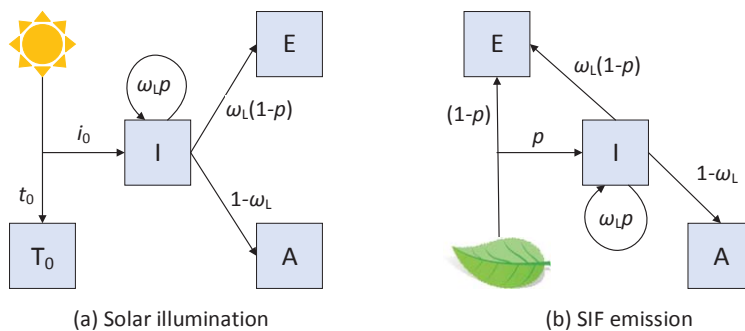
308 In this study, we used a *HyPlant* image acquired at 14:58 (local time) on June 30 2015 over the
309 study area located in the Ruhr catchment in the central western part of North Rhine-Westphalia,
310 Germany (50.864° N, 6.452° E). The flight height of 600 m above ground and the swath wide of ~ 400
311 m resulted in a spatial resolution of 1 m and view zenith angles from 0° to about 16.7° from the
312 center to the edges of the swath. The flight heading direction was 345.89°, under the solar zenith
313 angle of 31.89°, and the solar azimuth angle of 217.52°.

314 The far-red (760 nm) and red (687 nm) SIF at canopy level were retrieved using the iFLD
315 method ([Alonso et al. 2008](#)). A semi-empirical technique that made use of SIF-free reference pixels
316 (e.g., bare soil) was used to empirically account for uncertainties in estimated upward transmittance

317 of the atmosphere (Damm et al. 2014). For further technical details of SIF retrieval from the *HyPlant*
 318 image, please refer to Damm et al. (2014) and Wieneke et al. (2016). $fAPAR_{green}$ was estimated using
 319 the WDRVI-based linear model that was introduced in Section 2.2.4. As explained in Section 2.2.4, the
 320 linear relationship between $fAPAR_{chl}$ and $fAPAR_{green}$ was assumed also for the *HyPlant* image. The
 321 missing of information about chlorophyll content made it difficult to decide a proper coefficient for
 322 the $fAPAR_{chl}$ - $fAPAR_{green}$ relationship, so we did not calculate the $fAPAR_{chl}$ for the *HyPlant* image, but
 323 used the $fAPAR_{green}$ directly to evaluate the results of SIF downscaling.

324 2.4 Physical analysis of SIF radiation transfer within the canopy

325 The absorption and scattering of SIF photons within the canopy is ruled by the same physical
 326 interactions as in the case of the reflected radiation. The difference is only the location of the photons'
 327 source. SIF photons are emitted inside the leaves while, photons of reflected radiation originate from
 328 the solar illumination at the top of canopy (Figure 3).



329 Figure 3. An illustration of the canopy absorption and scattering model for solar illumination (a) and
 330 SIF emission (b) assuming with non-reflecting soil background. State T_0 represents photons that go
 331 through the canopy without interacting with the canopy or being absorbed by the soil; state I
 332 represents photons that interact with the canopy; state A represents photons absorbed by the canopy;
 333 and state E represents photons that escape from the canopy. p is the recollision probability, ω_L is

335 the leaf scattering coefficient (single scattering albedo), i_0 is the canopy interception of the
 336 incoming radiation, which means the probability of an incident photon that will be intercepted by the
 337 canopy, and t_0 is the probability that a photon can pass through the canopy without any
 338 interactions ($t_0 = 1 - i_0$).

339

340 Using the concept of recollision probability (so-called 'p-theory') (Stenberg et al. 2016) and
 341 assuming that the canopy is bounded underneath by a non-reflecting surface (the 'black-soil'
 342 condition), the four probable states of photons originating from solar illumination are as illustrated
 343 in Figure 3(a) (Smolander and Stenberg 2005). The canopy absorptance can be expressed as:

$$344 \quad a_i(\lambda) = i_0 \left[(1 - \omega_L(\lambda)) + \omega_L(\lambda)p(1 - \omega_L(\lambda)) + \omega_L(\lambda)^2 p^2(1 - \omega_L(\lambda)) + \dots \right] = i_0 \frac{1 - \omega_L(\lambda)}{1 - p\omega_L(\lambda)} \quad (7)$$

345 where p is the recollision probability, ω_L is the leaf scattering coefficient (single scattering albedo),
 346 and i_0 is the canopy interception of the incoming radiation. The canopy scattering can then be
 347 expressed as:

$$348 \quad s_i(\lambda) = i_0 - a_i(\lambda) = \frac{1-p}{1-p\omega_L(\lambda)} i_0 \omega_L(\lambda) \quad (8)$$

349 The recollision probability describes the multiple scattering process within the canopy. To
 350 describe the anisotropic escape probability of photons to leave the canopy, the bi-directional gap
 351 fraction, another spectral invariant, is needed. The term $(1 - p)$ can be expressed as the integrated
 352 canopy density over all directions in the unit sphere (Knyazikhin et al. 2013):

$$353 \quad 1 - p = \frac{1}{\pi} \int_{4\pi} \rho(\Omega) |\mu| d\Omega \quad (9)$$

354 where $\rho(\Omega)$ is the gap fraction for direction Ω , 4π denotes the unit sphere, and μ is the cosine of
 355 the polar angle of Ω . The canopy structure is the main factor influencing its reflectance anisotropy.

356 According to Knyazikhin et al. (2011 & 2013), the bi-directional reflectance factor (BRF),

357 representing the canopy scattering in a specific observing direction, can be approximately expressed
 358 as:

$$359 \quad \text{BRF}(\lambda, \Omega_s, \Omega_v) = \frac{\rho(\Omega_s, \Omega_v)}{1-p\omega_L(\lambda)} i_0 \omega_L(\lambda) \quad (10)$$

360 where $\rho(\Omega_s, \Omega_v)$ is the bi-directional gap fraction which contains the information of canopy
 361 structure and the fraction of sunlit and shaded leaves. Ω_s and Ω_v are the solar and view directions,
 362 respectively.

363 Similarly, for SIF emission, the probable states of the SIF photons emitted from leaves are as
 364 illustrated in Figure 3(b). It needs to be noted that, there is also probability for SIF photons to be
 365 absorbed by the soil without any interactions in the canopy (similar as the state of T_0 in Figure 3(a)).
 366 However, such probability is considered to be very low, because the SIF photons absorbed by soil
 367 directly are most likely from the bottom leaves, while the illumination on leaves at the bottom of
 368 canopy is usually very low for dense canopy. Additionally, for the red-band, the downward SIF at leaf
 369 level has been proved to be much weaker than the upward SIF (Van Wittenberghe et al. 2015).
 370 Therefore, the portion of SIF photons directly absorbed by the soil is neglected in this study.
 371 Accordingly, the canopy absorptance of SIF photons can be expressed as:

$$372 \quad a_f(\lambda) = p(1 - \omega_L(\lambda)) + \omega_L(\lambda)p^2(1 - \omega_L(\lambda)) + \omega_L(\lambda)^2p^3(1 - \omega_L(\lambda)) + \dots = p \frac{1-\omega_L(\lambda)}{1-p\omega_L(\lambda)} \quad (11)$$

373 and the canopy scattering of SIF photons as:

$$374 \quad s_f(\lambda) = 1 - a_f(\lambda) = \frac{1-p}{1-p\omega_L(\lambda)} \quad (12)$$

375 The scattering processes for SIF photons and for reflected photons by canopy elements are similar.
 376 Consequently, the SIF escape probability from leaf level to canopy level ($\varepsilon_{CL} = SIF_{Canopy}/SIF_{Leaves}$) in
 377 observing direction Ω can be expressed as:

$$378 \quad \varepsilon_{CL}(\lambda, \Omega) = \frac{\rho(\Omega)}{1-p\omega_L(\lambda)} \quad (13)$$

379 If we substitute Eq. (10) into Eq. (13), then we have,

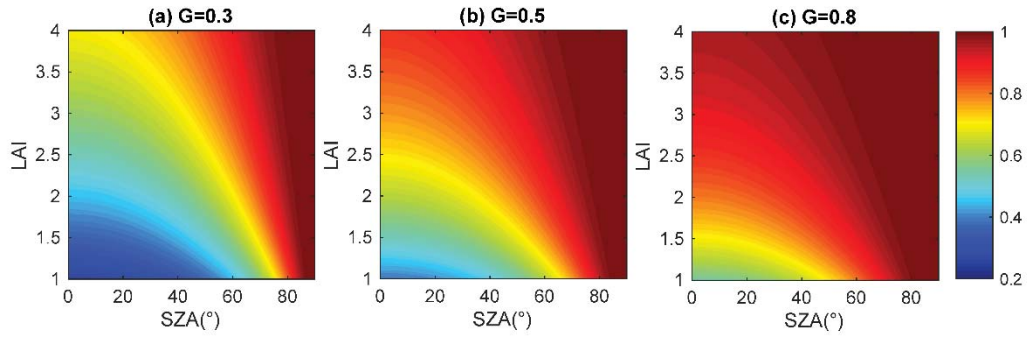
$$380 \quad \varepsilon_{CL}(\lambda, \Omega) = \frac{\text{BRF}(\lambda, \Omega)}{i_0 \omega_L(\lambda)} \quad (14)$$

381 According to the analysis above, under the 'black-soil' condition, the SIF escape probability from
382 leaf to canopy level is related to the directional reflectance, the canopy interception and the leaf
383 scattering coefficient. In practice, the directional reflectance can be acquired concurrently with the
384 SIF measurements, but canopy interception and leaf scattering coefficients can not, in general, be
385 accurately estimated. The canopy interception is driven by the canopy structure and the actual solar
386 position. If the clumping effect is assumed to be of minor impact, the canopy interception can be
387 expressed as (Chen and Black 1992; Ross 2012):

$$388 \quad i_0 = 1 - \exp\left(\frac{-G(\theta) \cdot LAI}{\cos(\theta)}\right) \quad (15)$$

389 where θ is the SZA and $G(\theta)$ is the mean projection coefficient for foliages on a plane
390 perpendicular to θ . The function, G , is determined by the LIDF. For the spherical leaf inclination
391 distribution type with an LIDF that is a sine function, the value of G is 0.5 and is independent of θ .
392 For other values of the LIDF, the value of G ranges from 0 to 1 when θ varies from 0° to 90° , and
393 generally converges to 0.5 when θ is approximately 57.3° for all LIDF types (Nilson 1971; Ross 2012;
394 Ryu et al. 2010). $G(\theta) \cdot LAI$ represents the projected LAI in the solar direction.

395 Figure 4 shows the values of i_0 for different values of G , LAI and SZA. For a dense canopy with
396 large values of LAI and G , the value of i_0 is close to 1, while for sparse canopies, the value of i_0 shows a
397 large degree of variability.



398

399

400

401

402

403

404

405

406

407

408

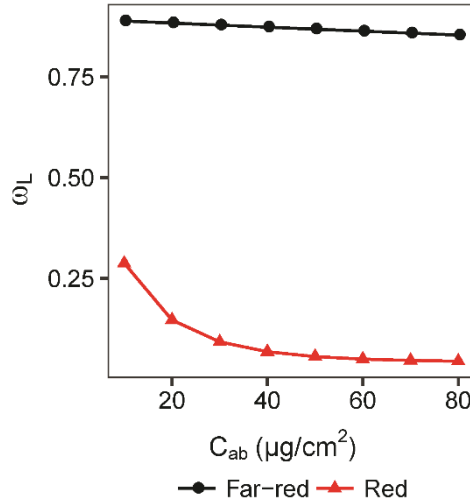
409

410

411

Figure 4. Values of the canopy interception of the incoming radiation (i_0) for different G function values, leaf area index (LAI) and solar zenith angle (SZA) combinations, calculated using Eq. (15). G function is the mean projection coefficient for foliages on a plane perpendicular to the solar zenith direction.

Since absorption by chlorophyll a molecules is very weak at the far-red band, leaf single scattering albedo (ω_L) is strongly influenced by chlorophyll content only in the red wavelengths of SIF emission. ω_L at the far-red band is, therefore, almost independent of chlorophyll content and it is driven by a minor absorptance of leaf tissue biochemical compounds. Figure 5 shows the variations of ω_L at the far-red (760 nm) and red (687 nm) bands simulated by the Fluspect model for leaf chlorophyll content from 10 to 80 $\mu\text{g}/\text{cm}^2$. As expected, the value of ω_L at the far-red band is almost invariant, reaching values between 0.853 and 0.888, while it varies from 0.044 to 0.287 for the red band, where the absorption by chlorophyll is strong. It exhibits a large variation in the value of ω_L , especially for the chlorophyll content lower than 40 $\mu\text{g}/\text{cm}^2$.



412

413 Figure 5. Values of ω_L at the far-red (760 nm) and red (687 nm) bands simulated by the Fluspect
 414 model for different values of the leaf chlorophyll content. The values for other input parameters for
 415 the Fluspect model were set as default (same as in Table 1).

416 Another fact needs to be noted is, the spectral invariant theory ignores the difference between
 417 the leaf reflectance and leaf transmittance (combined as ω_L). Therefore, the spectral invariant theory
 418 performs well at the far-red band, where multi-scattering dominates, but not so well at the red band,
 419 where single scattering dominates. Nevertheless, the ε_{CL} and $\frac{\text{BRF}}{i_0 \omega_L}$ are still proportional at the red
 420 band (Yang and Van der Tol. 2018). This problem is discussed in Section 4.4.

421 The escape probability for SIF from the PS level to the leaf level ($\varepsilon_{LP} = \text{SIF}_{\text{Leaves}}/\text{SIF}_{\text{PS}}$) is related
 422 to the leaf internal absorptance (from the photosystems to the leaf surface). The leaf internal
 423 absorptance at the spectral range of the SIF emission is caused mainly by the leaf chlorophyll content,
 424 but the relationship is non-linear, because the increment in radiation absorption per unit of
 425 chlorophyll decreases at high chlorophyll content (Adams et al. 1990; Gitelson et al. 1998;
 426 Porcar-Castell et al. 2014). Besides, chlorophyll molecules are distributed in different cell layers of
 427 leaf mesophyll tissues. Although the radiative transfer processes at the molecular-level are complex

428 for accurate modelling, ε_{LP} can be expressed as a non-linear function of the chlorophyll content (Cab)
429 and wavelength as:

$$430 \quad \varepsilon_{LP}(\lambda) \approx f(\text{Cab}, \lambda) \quad (16)$$

431 Consequently, the SIF escape probability from the PS level to the canopy level (ε_{CP}) can be
432 expressed as:

$$433 \quad \varepsilon_{CP}(\lambda, \Omega) = \varepsilon_{LP}(\lambda) \cdot \varepsilon_{CL}(\lambda) \approx f(\text{Cab}, \lambda) \cdot \frac{\text{BRF}(\lambda, \Omega)}{i_0 \omega_L(\lambda)} \quad (17)$$

434 To summarize, the SIF escape probability from the PS level to the canopy level can be
435 approximately modeled using the canopy BRF, canopy interceptance and Cab, under the assumption
436 of 'black-soil' condition. For remote sensing observations, the directional reflectance is available.
437 However, the i_0 and ω_L is not easy to be accurately measured or estimated. According to Eq. (15) and
438 Figure (4), i_0 is related to canopy structure, which is not easy to be accurately retrieved with optical
439 remote sensing approaches. It is not possible to observe leaf reflectance and transmittance directly at
440 canopy level, and ω_L varies among different leaves. So ω_L is also difficult to be estimated from
441 remote sensing observations at canopy level. But for a dense canopy and for leaves with a relatively
442 high value of Cab, i_0 and ω_L are relatively stable, and the directional reflectance is the main factor
443 that influences ε_{CP} , especially at the far-red band.

444 **2.5 Estimation of ε_{CP} and ε_{CL} using the random forest approach**

445 Given the difficulties involved in acquiring the parameters required for physical modelling of the
446 SIF downscaling, a statistical model based on the Random Forest (RF) regression, which is one of the
447 most effective machine learning models for predictive analytical approaches (Breiman 2011), was
448 trained on the dataset simulated in SCOPE to estimate ε_{CP} .

449 As shown in [Section 2.4](#), the BRF has significant impact on ε_{CP} . Taking all other factors together
450 as f_{CP} , Eq. (17) can be modified thus:

$$451 \quad \varepsilon_{CP}(\lambda, \Omega) = f_{CP} \cdot \text{BRF}(\lambda, \Omega) \quad (18)$$

452 where f_{CP} is the ratio of ε_{CP} to BRF. In the SCOPE simulations, $\varepsilon_{CP}(\lambda, \Omega)$ and $\text{BRF}(\lambda, \Omega)$ can be
453 simulated directly, and f_{CP} later calculated. As f_{CP} is acquired from SCOPE simulation instead of
454 physical analysis, the assumption of 'black-soil' condition for Eq. (17) is no longer needed here.
455 Similarly, ε_{CL} can be expressed as,

$$456 \quad \varepsilon_{CL}(\lambda, \Omega) = f_{CL} \cdot \text{BRF}(\lambda, \Omega) \quad (19)$$

457 We only estimated f_{CP} or f_{CL} with the random forest approach to increase robustness of estimated
458 ε_{CP} and ε_{CL} . Directional reflectance was obtained from measurements or simulations. f_{CP} and f_{CL} are
459 mainly related to the leaf scattering coefficient and canopy structure. These kinds of information can
460 be derived from directional reflectance at different bands and from various vegetation indices.

461 At the near infrared band, the canopy reflectance is dominated by the scattering effect, which
462 primarily originates from the leaf and canopy structure. At the red band, the canopy reflectance is
463 dominated by the absorption effect of chlorophyll pigments ([Colwell 1974](#); [Sims and Gamon 2002](#)). It
464 has been demonstrated that the red-edge band is important for the estimation of C_{ab} as it is less
465 impacted by the absorption saturation effect for a high C_{ab} than the red band ([Clevers and Gitelson](#)
466 [2013](#); [Dash and Curran 2004](#); [Gitelson et al. 2005](#); [Malenovský et al. 2013](#)). Several vegetation indices
467 (VIs), based on the reflectance at the red, red-edge and near infrared bands, have been developed for
468 the retrieval of vegetation parameters. In this study, the NDVI, simple ratio (SR) and the MERIS
469 terrestrial chlorophyll index (MTCI) were used (formulae and references in Table 5). Considering the
470 possible available wavelength range of spectral measurements for SIF retrieval, and to avoid the SIF

471 in-filling effect at the oxygen absorption bands at about 687 nm and 760 nm, we selected 685 nm as
 472 the red band, 710 nm as the red-edge band, and 758 nm as the near infrared band for the calculation
 473 of the Vis. The NDVI is sensitive to the canopy structural parameters such as LAI (Soudani et al. 2012).
 474 The SR is sensitive to the chlorophyll absorption at the red band. Finally, MTCI was designed for
 475 estimation of the chlorophyll content (Dash and Curran 2004). Consequently, NDVI, SR and MTCI,
 476 together with the canopy directional reflectance at 685 nm, 710 nm and 758 nm, were selected as the
 477 potential input variables to establish the RF regression. The scatter matrix of the relationships among
 478 the potential input variables and f_{CP} is provided in the Supplementary materials (Figure S1). The final
 479 selection of inputs was decided by testing the performance of RF regression with different
 480 combinations of the six potential variables, which is shown in Section 3.1.

481 Table 5. Mathematical formulations and references for the Vis (R_{758} , R_{685} and R_{710} stand for the
 482 directional reflectance at 758 nm, 685 nm and 710 nm, respectively).

Equation	Reference
$NDVI = (R_{758} - R_{685}) / (R_{758} + R_{685})$	(Rouse et al. 1973)
$SR = R_{758} / R_{685}$	(Jordan 1969)
$MTCI = (R_{758} - R_{710}) / (R_{710} - R_{685})$	(Dash and Curran 2004)

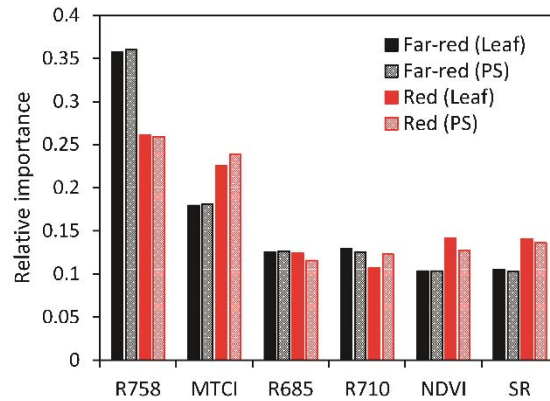
483
 484 500 decision trees were used to construct the RF model, and the minimum number of terminal
 485 nodes were set as 5. The SCOPE simulations (cf., Section 2.1.1), which cover most common vegetation
 486 conditions, were employed for the training of the RF. SIF of the red (687 nm) and far-red (760 nm)
 487 bands at canopy, leaf, and PS levels were simulated by the SCOPE model, together with the directional
 488 reflectance at 685 nm, 710 nm and 758 nm. Consequently, f_{CP} and f_{CL} could be calculated according to
 489 Eq. (18) and Eq. (19), respectively.

490

491 **3. Results**

492 **3.1 Selection of the inputs for the RF regression**

493 To optimize the inputs for the RF regression, we tested the performance of the RF model with
494 different combinations of the six potential input parameters explained in Section 2.5. Firstly, all the
495 six potential parameters were used as the inputs for the RF regression to calculate their relative
496 importance using the mean decrease accuracy (MDA) method based on the concept of out-of-bag
497 (OOB) error. The OOB error is a parameter that represents the RF prediction error. It is considered as
498 the mean prediction error on each training sample x_i , which uses only the trees that did not have x_i in
499 their bootstrap sample (Breiman, 2001). To measure the importance of the j -th feature for training,
500 the values of the j -th feature are permuted among the training data and the OOB error is computed
501 for each perturbed data set. The importance score for the j -th feature is computed by averaging the
502 difference in the OOB error before and after the permutation over all trees. Figure 6 shows the
503 relative importance of the input variables of the RF model for SIF downscaling from canopy level to
504 leaf level or PS level. These results indicate that the far-red directional reflectance and MTCI were
505 found as the most important variables for the SIF downscaling model at both the far-red and red
506 bands, while the importance of the directional reflectance at the red and red-edge bands, the NDVI,
507 and the SR was on similar, lower level.



508

509 Figure 6. Relative importance of input variables of the RF model for SIF downscaling from canopy

510 level to leaf level or PS level. R₇₅₈, R₆₈₅ and R₇₁₀ stand for the directional reflectance at 758 nm, 685

511 nm and 710 nm, respectively.

512 Secondly, the performance of the RF model was tested with different combinations of input

513 parameters. 2/3 of the SCOPE simulations were randomly selected to train the RF model, and the

514 remaining 1/3 were used as reference samples to evaluate the performance of the trained model with

515 the relative root-mean-square error with respect to mean value (RRMSE) and the coefficient of

516 determination (R²). To reduce the random errors, for each combination of input parameters, 30 RF

517 models were trained and the RRMSE and R² were averaged. The results are listed in Table 6. In

518 addition, a significance test was also carried out for further comparing the performance of different

519 combinations of input parameters (shown in Table S1). For the far-red band, when four parameters

520 (R₇₅₈, MTCl, R₆₈₅, R₇₁₀) were used, the RRMSE and R² became relatively stable, and the difference

521 comparing with using all six parameters became insignificant (the p-value is 0.273 and 0.335 for leaf

522 level and PS level, respectively). When adding more input parameters (SR and NDVI), the variation of

523 RRMSE was less than 0.5%. For the red band, in contrast, the difference between the performance of

524 using four input parameters (R₇₅₈, MTCl, R₆₈₅, R₇₁₀) and using all six parameters was still significant

525 for both leaf level and PS level (p-value < 10⁻⁹, see Table S1). When adding SR or NDVI as the input
 526 parameters, the RRMSE of the RF model was improved clearly (the RRMSE was reduced about 10%
 527 for the leaf level and about 6% for the PS level). But the performance of the RF model had no
 528 significant improvement when using both SR and NDVI (p-values > 0.300, see Table S1). The results
 529 also indicated that, although the vegetation indices can be calculated using the reflectance at the
 530 three wavelengths, they can still provide important information for the estimation of f_{CL} and f_{CP} ,
 531 because vegetation indices are able to enhance some information by non-linearly combining the
 532 reflectance at different wavelengths, and the special non-linear relationship may be difficult for the
 533 RF regression to find out.

534 According to the results, R_{758} , MTCI, R_{685} , and R_{710} were selected as the input parameters of the
 535 RF model for the estimation of f_{CL} and f_{CP} at the far-red band, while R_{758} , MTCI, R_{685} , R_{710} , and SR were
 536 selected for the red band.

537 Table 6. The relative root-mean-square error (RRMSE) and the coefficient of determination (R^2) of RF
 538 models for the ratios of SIF escape probability to BRF (f_{CL} for leaf level to canopy level and f_{CP} for
 539 photosystem level to canopy level) at far-red and red bands with different combinations of input
 540 parameters.

Input parameters	f_{CL} (Far-red)		f_{CP} (Far-red)		f_{CL} (Red)		f_{CP} (Red)	
	RRMSE	R^2	RRMSE	R^2	RRMSE	R^2	RRMSE	R^2
R_{758} , R_{710} , R_{685}	0.0492	0.871	0.0569	0.901	0.0981	0.960	0.0942	0.954
R_{758} , MTCI, R_{685}	0.0463	0.886	0.0502	0.928	0.0990	0.961	0.0969	0.957
R_{758} , MTCI, R_{685} , R_{710}	0.0462	0.886	0.0489	0.931	0.0871	0.964	0.0849	0.961
R_{758} , MTCI, R_{685} , R_{710} , SR	0.0461	0.887	0.0487	0.931	0.0804	0.968	0.0797	0.964
R_{758} , MTCI, R_{685} , R_{710} , NDVI	0.0463	0.886	0.0488	0.930	0.0800	0.969	0.0797	0.964
R_{758} , MTCI, R_{685} ,	0.0461	0.887	0.0487	0.931	0.0799	0.969	0.0795	0.966

541

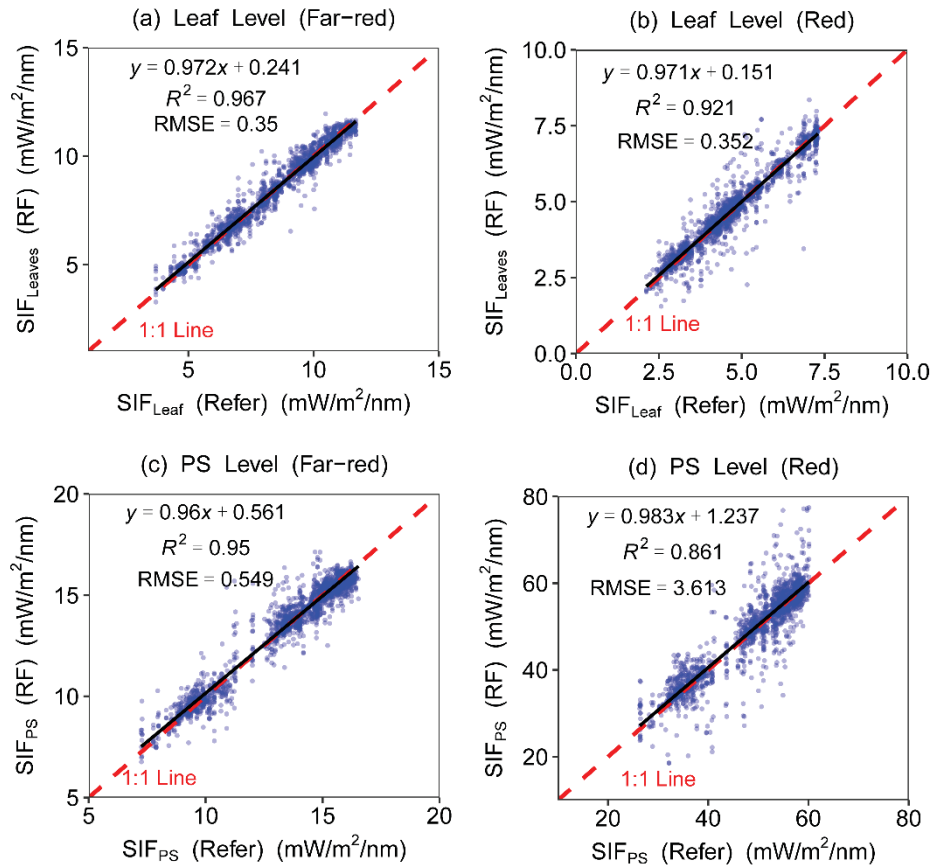
542 **3.2 Evaluation of the SIF downscaling accuracy using SCOPE and DART simulations**

543 SCOPE and DART based simulations were used in the first instance to quantitatively evaluate the
544 performance of the RF approach for SIF downscaling. SCOPE allows simulating SIF values at the
545 canopy, leaf, and PS levels, but there is no module for SIF simulation at PS level in DART, so the DART
546 model is only able to provide the SIF values at the canopy and leaf levels.

547 The SCOPE simulations were first used for accuracy assessments at the leaf and PS levels. 2/3 of
548 the SCOPE simulations were randomly selected to train the RF model, and the remaining 1/3 was
549 used for validation. Figure 7 shows a comparison of the far-red and red SIF estimated by the RF
550 approach with the reference SIF simulated by SCOPE for the leaf and PS levels. In general, the
551 estimated values of SIF at the leaf and PS levels matched well with the reference values. Most of the
552 points were located near to the 1:1 line, and the values of the coefficient of determination (R^2) were
553 higher or close to 0.9. The estimation of red SIF at the PS level was not as robust as that of the far-red
554 SIF, but the root-mean-square error (RMSE) was still as low as 3.613 mW/m²/nm, resulting in the
555 relative root-mean-square error (RRMSE) of 7.299%. The relationship of SIF at canopy level and leaf
556 level, SIF at leaf level and PS level, SIF at canopy level and PS level from SCOPE simulations are also
557 provided in the Supplementary materials (Figure S2) for comparisons.

558

559



560

561

562 Figure 7. Comparison of far-red (760 nm) and red (687 nm) SIF estimated by the RF approach with
 563 reference SIF simulated by SCOPE for leaf and PS levels. R^2 is the coefficient of determination, and
 564 RMSE is the root-mean-square error.

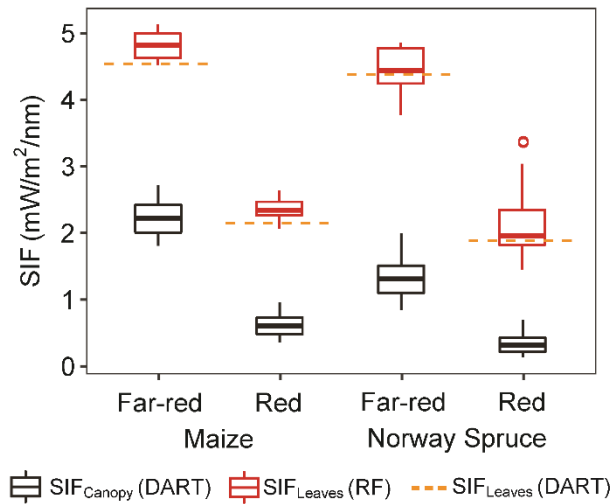
565

566 Simulations performed in the 3-D DART model (cf., [Section 2.1.2](#)) were used for further
 567 evaluation of the RF model trained by the SCOPE simulations. Since DART produced canopy and leaf
 568 SIF simulations for two modeled canopies of maize and spruce, only the downscaling of SIF from the
 569 canopy level to the leaf level could be evaluated. Figure 8 shows SIF simulated by DART at canopy and
 570 leaf level vs. estimates of downscaled SIF. The leaf SIF estimates for the maize canopy were more
 571 robust (less variable) for the spruce canopy, but the downscaled estimates matched well the

572 reference values in both cases. The RRMSE between the estimated and reference far-red and red leaf
 573 SIF was 7.42% and 12.10% for the maize canopy, and 7.57% and 25.92% for the spruce canopy.

574

575



576

577 Figure 8. Boxplot of far-red (740 nm) and red (687 nm) SIF simulated by DART for maize and spruce
 578 canopies and corresponding downscaled leaf SIF using the Random Forest (RF) model. The orange
 579 dashed line shows the reference values of SIF at leaf level, as simulated in DART by Fluspect. The
 580 bottom and top of each box represent the first and third quartiles, respectively, the thick horizontal
 581 line in the box is the median, the whiskers show the maximum/minimum values within 1.5 times the
 582 interquartile range (IQR, the difference between the third and the first quartiles), and the circles
 583 show the outliers out of 1.5IQR. The units of $\text{mW}/\text{m}^2/\text{nm}/\text{sr}$ were applied to SIF at canopy level as
 584 well as leaf level to make the values comparable.

585

586 The evaluation carried out on datasets simulated by two different radiative transfer models
 587 using different vegetation representations and solar-viewing geometries revealed accurate and

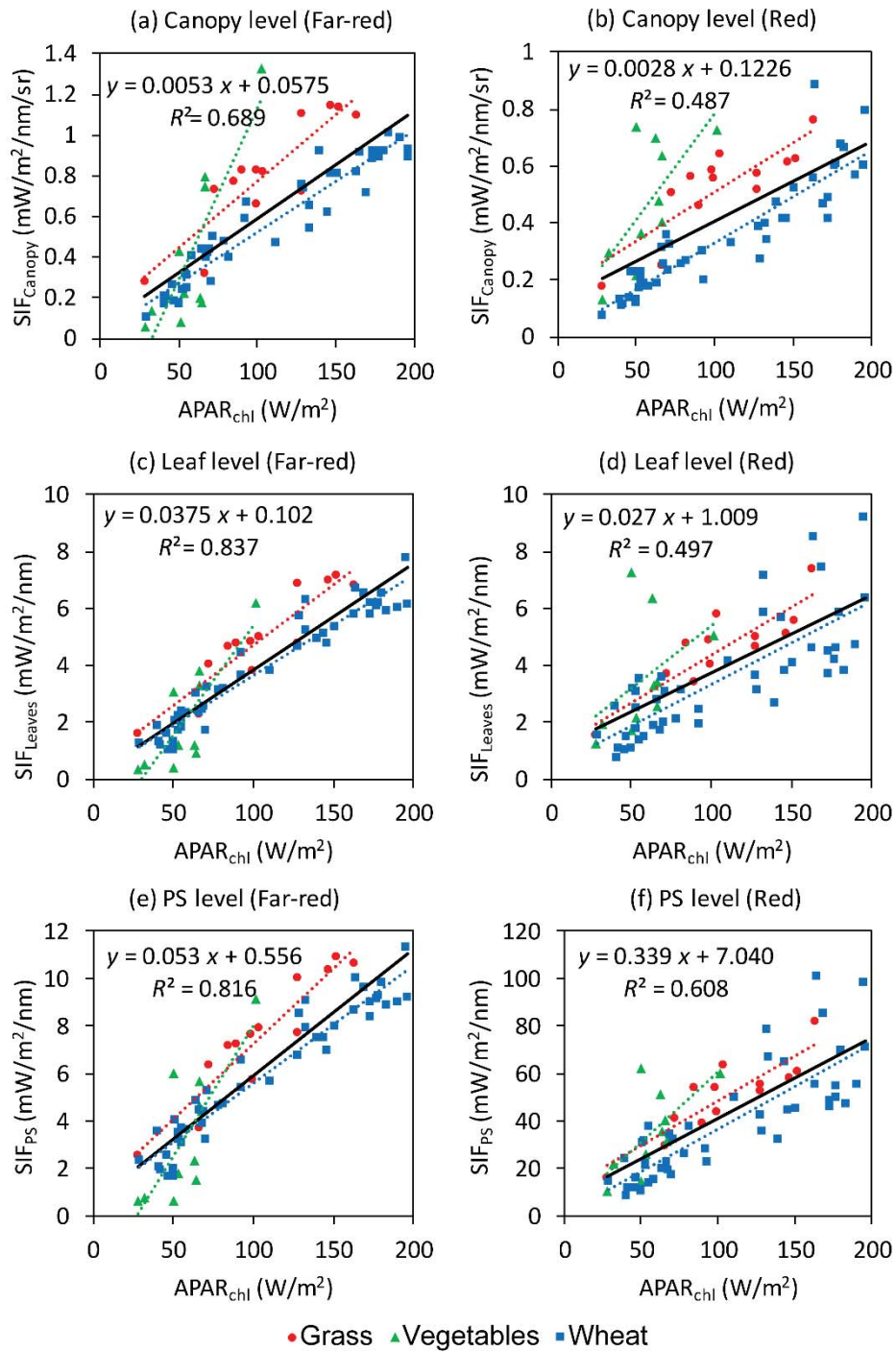
588 robust performance of the RF downscaling approach, especially for the far-red SIF. The lower
589 accuracy for the red band is discussed in Section 4.4.

590 **3.3 Evaluation of SIF downscaling through in-situ multi-species experiments**

591 Under conditions with no stress and with high light, the SIF yield varies little (Van der Tol et al,
592 2014; Damm et al. 2015), so the total SIF emission of a plant at PS level is strongly related to $APAR_{chl}$.
593 However, SIF at the canopy level is strongly influenced by re-absorption and scattering effects, which
594 are related to leaf pigments and the canopy structure. Therefore, we compared $APAR_{chl}$ measured for
595 multi-species canopies of different structures with SIF downscaled to PS level with the RF approach
596 (cf., Section 2.2.1).

597 Figure 9 shows the relationship between $APAR_{chl}$ and nadir-observed canopy SIF, SIF at leaf level
598 and SIF at PS level estimated by the RF approach. The relationship between $APAR_{chl}$ and SIF_{canopy}
599 varied for different species, while the slope of the linear regression lines of the SIF- $APAR_{chl}$ models for
600 different species became closer to each other when SIF was downscaled from canopy level to PS level,
601 which indicated that the relationship between $APAR_{chl}$ and SIF_{PS} was less species-dependent. At the
602 far-red band, the values of R^2 increased significantly when SIF was downscaled from canopy level to
603 leaf level, but did not vary much (decreased a little) when SIF was further downscaled to the PS level.
604 Differently, at the red band, the R^2 for the PS level was much higher than that for the leaf level.

605



606

607 Figure 9. The relationship between $APAR_{chl}$ and canopy SIF observed at nadir (a, b), SIF at leaf level (c,

608 d) and PS level (e, f) estimated by the RF approach for several different species (grass, various

609 vegetables and wheat). The colored dash lines are the linear regression lines for specific species. The

610 black solid lines and the equations are the linear regression lines and models for all the samples.

611

612 Table 7. Linear regression models of the SIF-APAR_{chl} relationship for different species at canopy, leaf

613 and photosystem (PS) levels. The 'CV of slopes' are the coefficients of variation of the slopes for

614 different species at specific levels.

Band	Level	Grass	Vegetables	Wheat	CV of slopes
Far-red	Canopy	$y = 0.0065x + 0.122$ $R^2 = 0.7873$	$y = 0.017x - 0.5606$ $R^2 = 0.7078$	$y = 0.005x + 0.0213$ $R^2 = 0.9182$	0.688
	Leaf	$y = 0.0423x + 0.468$ $R^2 = 0.8567$	$y = 0.0778x - 2.3764$ $R^2 = 0.6803$	$y = 0.0352x + 0.1319$ $R^2 = 0.9292$	0.441
	PS	$y = 0.0634x + 0.8884$ $R^2 = 0.8786$	$y = 0.1108x - 3.0645$ $R^2 = 0.6122$	$y = 0.0495x + 0.6585$ $R^2 = 0.9227$	0.431
Red	Canopy	$y = 0.0035x + 0.1653$ $R^2 = 0.7068$	$y = 0.0074x + 0.0417$ $R^2 = 0.4672$	$y = 0.0033x + 0.0056$ $R^2 = 0.8232$	0.488
	Leaf	$y = 0.0336x + 0.9976$ $R^2 = 0.7621$	$y = 0.0444x + 0.9485$ $R^2 = 0.1964$	$y = 0.0292x + 0.4097$ $R^2 = 0.6182$	0.219
	PS	$y = 0.3808x + 10.094$ $R^2 = 0.7719$	$y = 0.5914x + 1.3347$ $R^2 = 0.4455$	$y = 0.358x + 1.031$ $R^2 = 0.6831$	0.290

615 The linear regression models of the SIF-APAR_{chl} relationship for different species at canopy, leaf

616 and PS levels were summarized in Table 7, and the coefficients of variation (CV) of the slopes for

617 different species at each level were also calculated. For grass and wheat, the relationships between

618 SIF at all levels and APAR were close to linear. But for the vegetation, the relationship was some

619 erratic, especially at the red band. The reason may partly due to the measurement errors. For both

620 the far-red and red bands, the CV of slopes for different species decreased significantly when SIF was

621 downscaled from canopy level to leaf or PS level. At the far-red band, both the CV of slopes and the R²

622 of each model at the PS level were very close to that at the leaf level. At the red band, the CV of slopes

623 at the PS level was some higher than that for the leaf level, but the R² of the regression model for all

624 the three species were higher than that at the leaf level, especially for the model of the vegetables

625 (increased from 0.1964 to 0.4455 when SIF was downscaled from leaf level to PS level).

626

627 The results shown in Figure 9 and Table 7 confirmed that the species-dependency of the
628 SIF-APAR_{chl} relationship could be reduced by SIF downscaling from canopy level to leaf or PS level.
629 These results also indicated that the canopy structure is the main factor influencing the far-red SIF
630 escape probability, while the leaf internal absorption mainly influence the red SIF.

631 **3.4 Evaluation of SIF downscaling using multi-angular experiments**

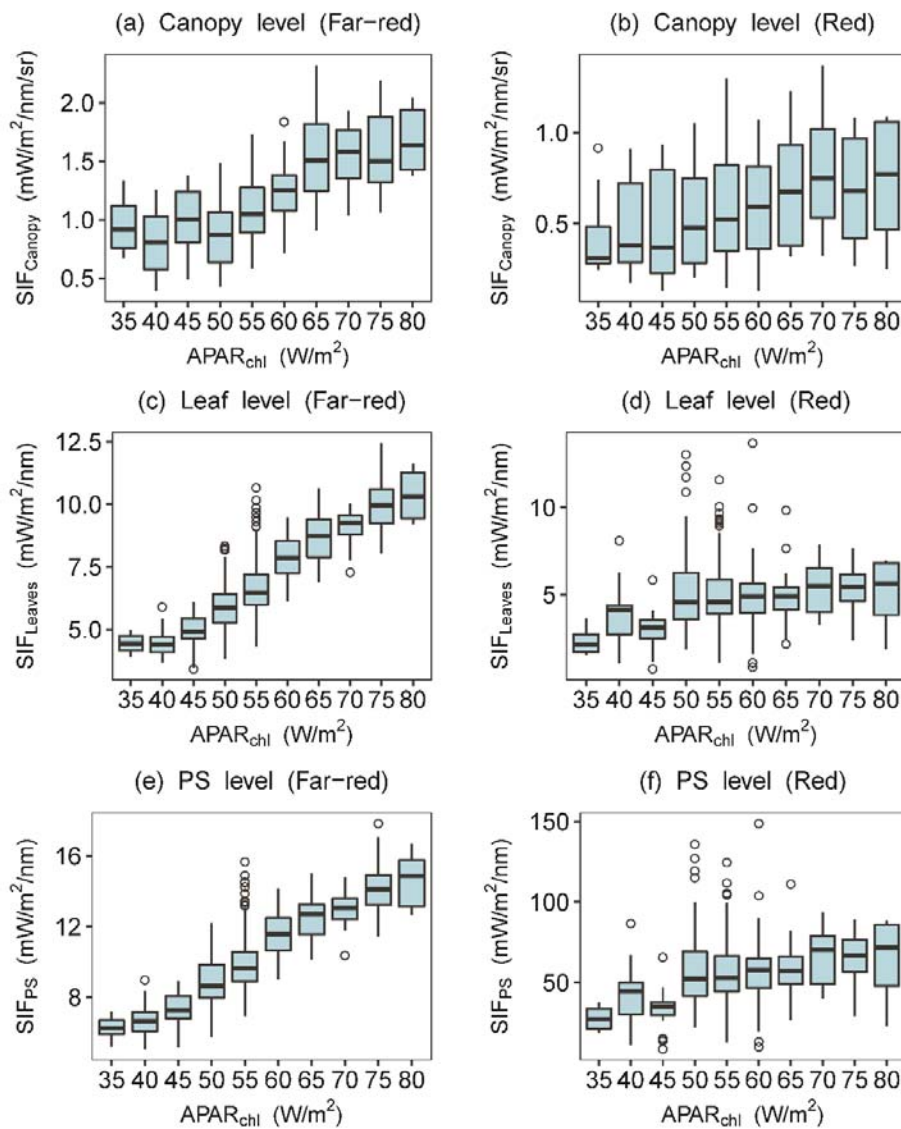
632 The SIF emission at the PS level can be regarded as isotropic whereas, due to re-absorption and
633 scattering within the canopy, the observed SIF at the canopy level is obviously anisotropic.
634 Consequently, multi-angular measurements of a winter wheat canopy (cf., [Section 2.2.2](#)) were used
635 for further evaluation of the SIF downscaling approach, in particular its potential to normalize the
636 anisotropy in the SIF measurements.

637 Figure 10 shows the relationship between APAR_{chl} and values of the multi-angular observed SIF
638 at canopy level, leaf level or PS level in the form of boxplots. The APAR_{chl} values were divided into
639 groups with an interval of 5W/m². Moreover, for each set of multi-angular observations (with
640 different VZAs in the solar principal plane), we calculated the coefficients of variation (CV) of SIF at
641 canopy level, leaf level or PS level, as shown in Figure 11. Lower CV values indicated less anisotropy
642 of SIF. The results shown in Figure 10 and Figure 11 demonstrate that, for each APAR_{chl} level, SIF at
643 canopy level varied substantially at both the far-red and red bands due to its anisotropic
644 characteristics caused by the scattering within the canopy. Computed CV values varied from 0.12 to
645 0.32 for the far-red band, and from 0.33 to 0.61 for the red band. The value of R² for the relationship

646 between SIF_{Canopy} and $APAR_{chl}$ is 0.43 and 0.09 for the far-red band and the red band, respectively. The
647 estimated SIF at the leaf level and PS level was much more closely related to $APAR_{chl}$ and the variation
648 of SIF in predefined $APAR_{chl}$ level was visibly reduced. At the far-red band, the value of R^2 for the
649 relationship between SIF_{PS} and $APAR_{chl}$ was 0.76, and the values of CV for SIF_{PS} varied from 0.04 to
650 0.18. At the red band, there were some outliers in the boxplot which indicates a less robust
651 performance of the SIF downscaling. Overall, the value of R^2 for the relationship between SIF_{PS} and
652 $APAR_{chl}$ was 0.14, and the values of CV for SIF_{PS} for most sets of multi-angular observations were also
653 reduced and lie within the range 0.14 to 0.42. The results for SIF downscaling to leaf level and to PS
654 level were very similar; because the leaf absorptance did not vary a lot (the chlorophyll contents for
655 all the samples were very similar as shown in Table 4). The results also confirmed the assumption
656 that the SIF emission at both leaf level and PS level is isotropic.

657

658



659

660 Figure 10. The relationship between $APAR_{chl}$ and multi-angular observations of SIF at canopy level (a,

661 b) and estimated SIF at leaf level (c, d) or PS level (e, f) by the RF approach. The bottom and top of the

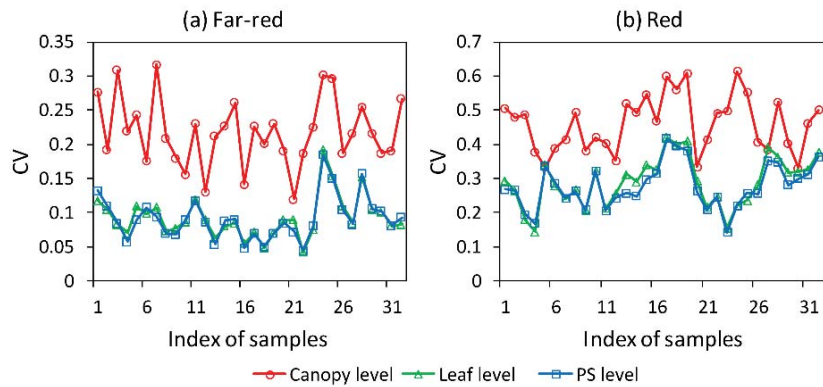
662 boxes correspond to the first and third quartiles, the thick horizontal line in each box is the median,

663 the whiskers show the maximum/minimum values within 1.5 IQR, and the circles show the outliers

664 that lie outside 1.5 IQR. The multi-angular observations were conducted on a wheat canopy. The

665 averaged number of observations per APAR interval is 49.

666



667

668 Figure 11. The coefficients of variation (CV) of the observed canopy SIF and leaf or PS SIF estimated
 669 by the RF approach for each set of multi-angular observations in the solar principal plane. Each
 670 sample was calculated using a set of multi-angular observations taken within 7 minutes and the SIF
 671 at PS level was expected to be constant.

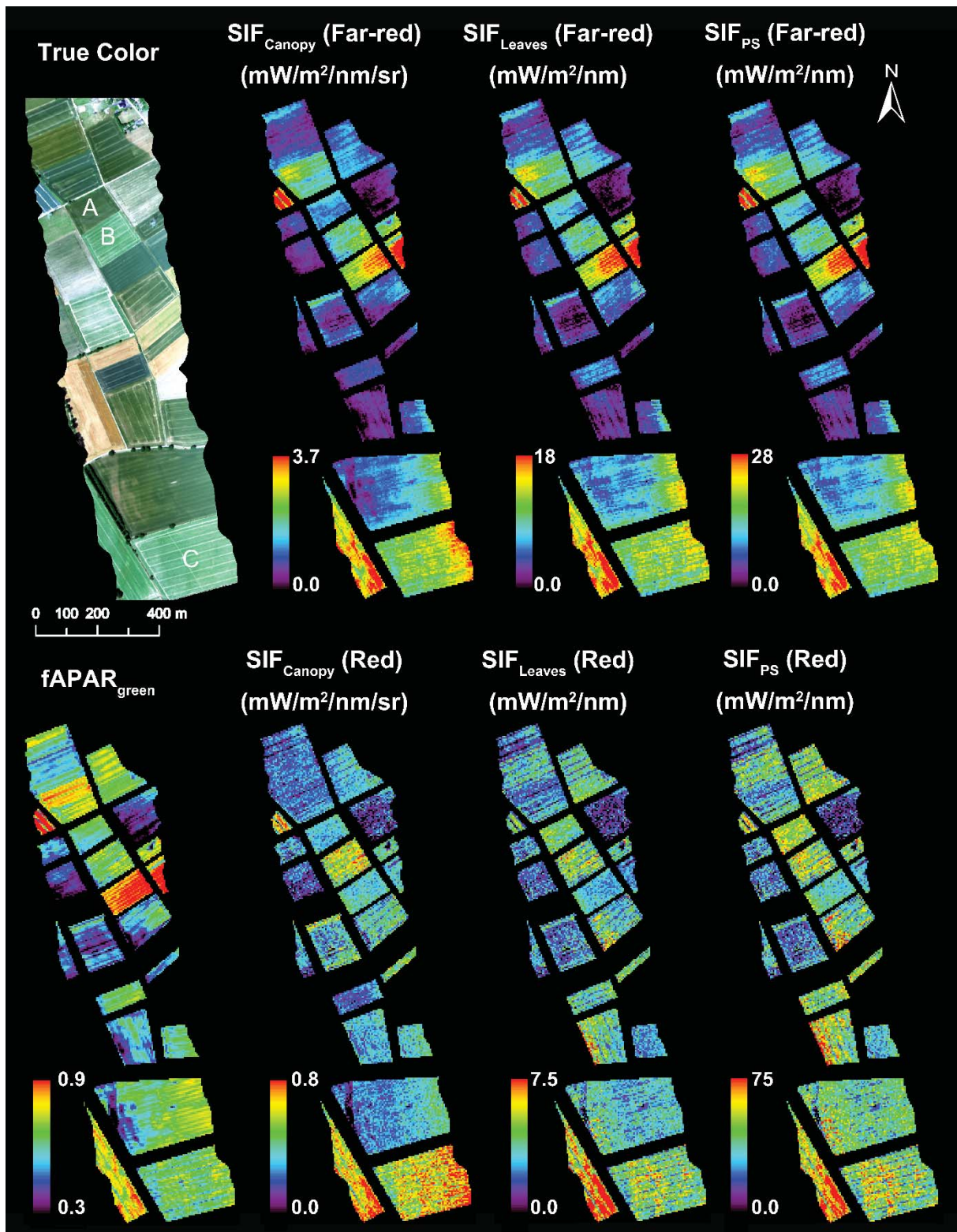
672

673

674 3.5 Downscaling of canopy SIF retrieved from *HyPlant* image

675 Besides the ground-based measurements, in this study, a *HyPlant* image was also employed for
 676 the evaluation of the SIF downscaling results. Before application of SIF downscaling, the original pixel
 677 size of the *HyPlant* was reduced from 1 m × 1 m to 5 m × 5 m in order to reduce the influence of
 678 sensor noise.

679



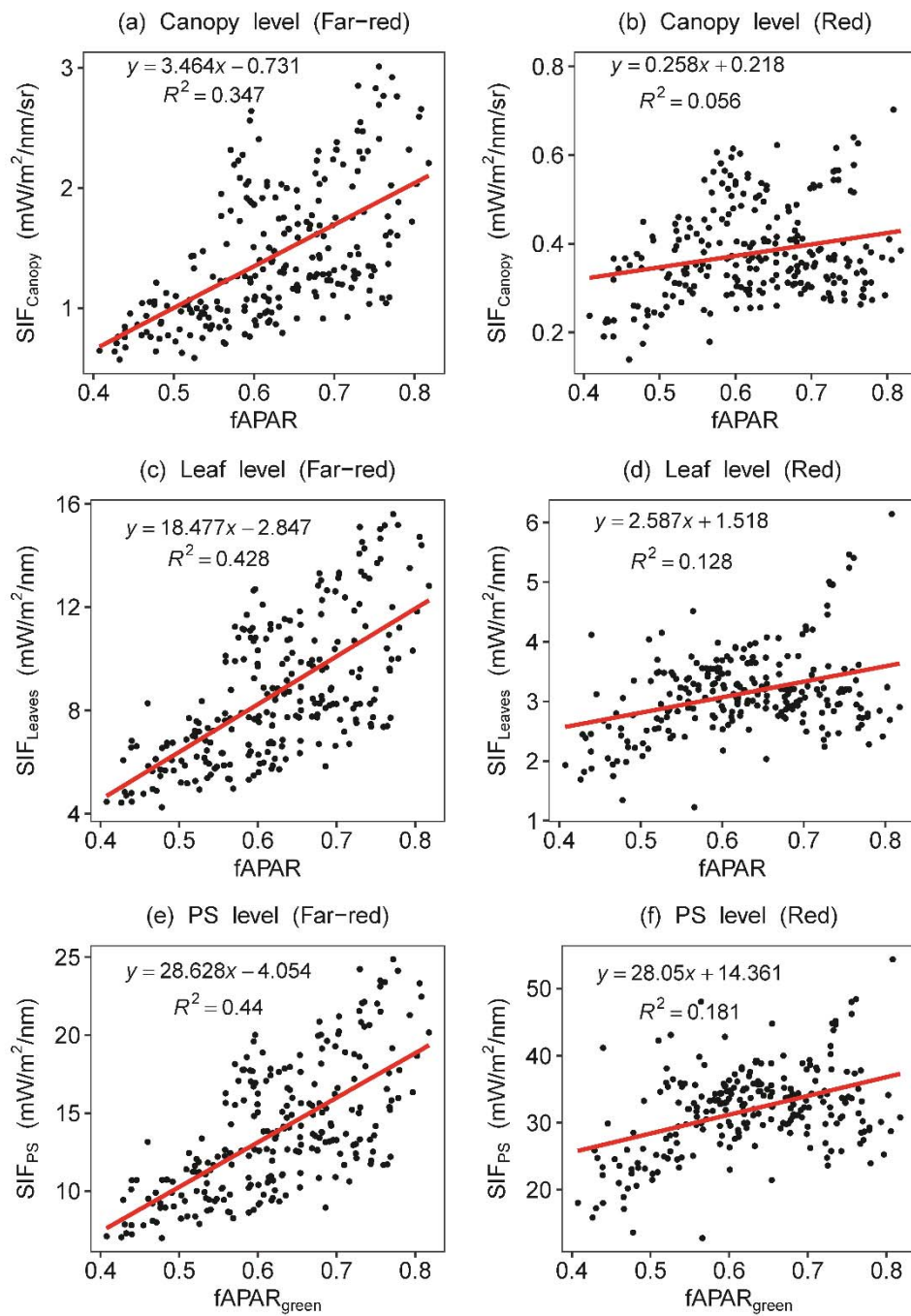
680

681 Figure 12. True color composited *HyPlant* image and values of $fAPAR_{green}$, SIF at canopy level

682 (retrieved using the iFLD method), SIF at leaf level and PS level (estimated using the RF approach) at

683 both the far-red (760 nm) and red (687 nm) bands. The image was acquired at 14:58 (local time) on

684 June 30 2015 over the study area located in the Ruhr catchment in the central western part of North
685 Rhine-Westphalia, Germany (50.864° N, 6.452° E). The flight height was 600 m above ground. The
686 species in the fields labeled as "A", "B" and "C" in the true color image are winter wheat, potato and
687 sugar beet, respectively. The three fields are selected as examples for further analysis.
688



689

690 Figure 13. Relationship between $fAPAR_{green}$ and SIF at canopy level, leaf level and PS level retrieved

691 from the HyPlant image. Non-vegetation pixels were excluded. In order to reduce the propagation of

692 noise, each point represents the averaged pixel value in a $50\text{ m} \times 50\text{ m}$ window.

693

694 Next to the true color composite of the *HyPlant* image, Figure 13 shows $fAPAR_{green}$, canopy SIF
695 retrieved by the iFLD method, and SIF at leaf and PS levels as estimated by the RF approach for both
696 far-red and red bands. In Figure 12, an obvious variation in the value of ϵ_{CP} for the different fields
697 can be seen. As an example, *Field A* (winter wheat) and *Field B* (potato) feature similar levels of
698 $fAPAR_{green}$ and SIF_{PS} but their SIF_{canopy} were quite different, which indicated significant differences in
699 their canopy structure (see the color of *Field A* and *Field B* in the true color image in Figure 12). Their
700 different relationships between $fAPAR_{green}$ and SIF_{canopy} could be attributed to the differences in ϵ_{CP} .
701 Moreover, the *HyPlant* results also demonstrated that the SIF anisotropy at canopy level was
702 efficiently corrected after the downscaling. For example, as shown in the image, despite a relative
703 spatial visual homogeneity of *Field C* (see the true color image in Figure 12), the map of SIF_{canopy}
704 showed a systematically increasing trend from west to east. The view zenith angle for *HyPlant* varied
705 from -16.7° to $\sim 16.7^\circ$ for pixels from the left to the right of the swath and so this variation in SIF_{canopy}
706 within a homogeneous field may be related to SIF anisotropy. In contrast, the value of SIF_{PS} in this
707 field was much more homogeneous.

708 Relationship between $fAPAR_{green}$ and SIF at canopy, leaf or PS level extracted from the *HyPlant*
709 image vegetation pixels were presented in Figure 13. Although the spatial resolution of the *HyPlant*
710 image was reduced from 1 m to 5 m, the SIF images still appear noisy, especially for the red band. To
711 further reduce the noise influence, we aggregated image pixels into $50\text{ m} \times 50\text{ m}$ bins, in which the
712 $fAPAR_{green}$ and SIF values were averaged (the scatter plots for the $5\text{ m} \times 5\text{ m}$ images are available in
713 the Supplementary materials (Figure S3)). Since the *HyPlant* image used in this study was acquired
714 within one minute and the study area was flat, the PAR was expected to be constant for all pixels. The
715 graphs showed a stronger and more linear relationship between SIF_{PS} and $fAPAR_{green}$ than between

716 SIF_{Canopy} and fAPAR_{green} for both the far-red band and the red band. The downscaling of SIF from
717 canopy to PS level using the RF approach has increased the value of R² for the linear relationship
718 between SIF and fAPAR_{green} from 0.347 to 0.440 at the far-red band, and from 0.056 to 0.181 at the
719 red band. For the far-red band, values of R² for the leaf level and PS level were very similar, while for
720 the red band, the value of R² for the PS level was higher than that for the leaf level.

721 **4. Discussion**

722 **4.1 Downscaling of SIF for the correction of SIF anisotropy**

723 The observed SIF anisotropy at the canopy level is due to the re-absorption and scattering effects
724 within the canopy. [Guanter et al. \(2012\)](#) and [Joiner et al. \(2012\)](#) reported the influence of the
725 sun-view geometry on satellite remotely sensed SIF. Since the upwelling radiative transfer process
726 from leaf level to canopy level for SIF emission is similar to that of reflected radiation, one can assume
727 that SIF anisotropy is similar to that of reflectance ([Liu et al. 2016](#)).

728 According to the physical analysis of the SIF radiative transfer within the canopy conducted in
729 this study, which was neglecting the influence of soil reflectance (is applicable for dense canopies),
730 the SIF anisotropy at canopy level can be normalized by the BRF as expressed by Eq. (14), which is
731 consistent with [Liu et al. \(2016\)](#). Multi-angular measurements of a winter wheat canopy were used in
732 the evaluation of the SIF downscaling (Figure 11 and Figure 12). The results showed that, after the
733 downscaling process, the difference in the values of SIF observed at different VZAs was reduced
734 effectively. Similarly, in the *HyPlant* image, due to the variation of view zenith angle, SIF at canopy
735 level showed obvious differences between the center and edges of the swath, while SIF at PS level was

736 more homogeneous within each field.

737 [Pinto et al. \(2017\)](#) showed the angular distribution of SIF emission of a sugar beet canopy which
738 consistent with our DART simulations shown in Figure 1, and they pointed out that the directional
739 SIF emission is related to the canopy structure. [He et al. \(2017\)](#) developed a model to normalize the
740 remotely sensed SIF to the hot spot direction by quantifying the fraction of sunlit and shaded leaves
741 in the field of view, and consequently, the total SIF at canopy level could be estimated as a weighted
742 sum of SIF from sunlit and shaded leaves. They reported that the calculated total SIF was better
743 related with the simulated total GPP than the original SIF observation. According to these relevant
744 studies, the demonstrated SIF directional correction is especially important for long-term,
745 ground-based or satellite-based observations of SIF time series as the sun-view geometry has a big
746 influence on the SIF values ([Guanter et al. 2012](#); [Joiner et al. 2012](#); [Liu et al. 2016](#); [He et al. 2017](#);
747 [Pinto et al. 2017](#)). The downscaling approach proposed in this paper presents a practical method of
748 reducing the anisotropy of SIF emissions, which consequently enables less biased understanding of
749 the SIF information at canopy level.

750 **4.2 Improvements of APAR estimation by SIF downscaling**

751 APAR is a bridge linking SIF to GPP ([Berry et al. 2012](#); [Porcar-Castell et al. 2014](#)). Besides the SIF
752 anisotropy at the canopy level, the SIF-APAR relationship also depends on the canopy components
753 and structures.

754 [Du et al. \(2017\)](#) studied the response of SIF to $APAR_{chl}$ using a simulated dataset and ground
755 measurements, and found that the relationship between SIF_{Canopy} and $APAR_{chl}$ is highly dependent on
756 the canopy structure and chlorophyll content, especially for the red band. Our study pointed out that

757 corrections for the re-absorption and scattering that affects the SIF transfer from the PS level to
758 canopy level is important for linking SIF_{Canopy} to $APAR_{\text{chl}}$. The study by [Guanter et al. \(2014\)](#) also
759 found that there are differences between SIF-GPP models relationships for US croplands and
760 European grasslands. According to the multi-species experiments used in our study (Figure 10), the
761 RF-based downscaling of SIF is efficient to reduce the influence of the re-absorption and scattering
762 effects within the canopy, and to reduce the species-dependency of the SIF- $APAR_{\text{chl}}$ models.

763 [Wieneke et al. \(2016\)](#) analyzed the value of F_{yield} at canopy level ($SIF_{\text{Canopy}}/APAR$) for different
764 agricultural fields captured in a *HyPlant* image, and found that F_{yield} varied with the crop type and
765 with the time of image acquisition, i.e., the solar zenith and azimuth angles. The reason could be
766 partly related to the re-absorption and scattering of SIF within the canopy. The results that we
767 obtained using the *HyPlant* image further support the idea that SIF downscaling from canopy level to
768 PS level can help to achieve more stable and reliable SIF-based APAR models.

769 **4.3 The variation of SIF spectral shape at canopy, leaf and PS levels**

770 Apart from the intensity of single-wavelength SIF, the spectral shape of SIF also contains
771 important information ([Liu et al. 2015](#)). The two photosystems, PS I and PS II, contribute differently
772 to the SIF emission. The PS II is responsible for the SIF emission at both the red and far-red bands,
773 while the PS I only contributes to the far-red SIF emission and has a much smaller yield ([Pfündel](#)
774 [1998](#); [Agati et al. 2000](#)). Therefore, the spectral shape of SIF is related to the energy distribution
775 between PS I and PS II ([Porcar-Castell et al. 2014](#)). However, as the within-canopy re-absorption and
776 scattering effects on SIF are quite different for the red band and the far-red band, the spectral shape
777 of SIF at canopy, leaf and PS levels varies significantly ([Fournier et al. 2012](#); [Moya et al. 2006](#);

778 [Porcar-Castell et al. 2014](#)). [Romero et al. \(2018\)](#) developed a model based on the canopy reflectance,
779 canopy transmittance and soil reflectance to retrieve the spectral shape of fluorescence emission at
780 leaf level from the observed fluorescence at canopy level. [Ramos and Lagorio \(2004\)](#) proposed a
781 physical model to obtain the fluorescence spectra at PS level by combining the leaf fluorescence
782 emission and leaf reflectance. Based on the two studies above, it is possible to retrieve the SIF
783 spectral shape at PS level from SIF observation at canopy level, but the absolute intensity of SIF
784 emission at leaf level or PS level is not available.

785 In this paper, although we focused on the SIF downscaling at two spectrally narrow bands
786 instead of full-wavelength, it is still possible to see the variation of SIF spectral shape at canopy, leaf
787 and PS levels using the ratio of far-red and red SIF. For the wheat canopy introduced in the
788 multi-species experiment, the averaged ratios of SIF at the far-red band (760 nm) and red band (687
789 nm) are 1.63, 1.17 and 0.17 for the canopy level, leaf level and PS level, respectively. The significant
790 decrease of the SIF ratios results from a much stronger re-absorption effect at the red band. The
791 results are consistent with the Figure 8 in [Romero et al. \(2018\)](#).

792 **4.4 Reliability of this study**

793 A practical solution based on RF regression was proposed to overcome the difficulties in the
794 physical approach for SIF downscaling from canopy level to PS level. As an efficient machine learning
795 algorithm, the RF regression model is able to give accurate prediction of parameters if it is properly
796 trained. The RF model is made up of a large number of decision trees. Each decision tree is
797 independently grown on a bootstrap sample, and hence, the trees are weakly correlated. Therefore,
798 the risk of overfitting the training dataset, which is a significant problem for many machine learning

799 algorithms, can be reduced ([Abdel-Rahman et al. 2013](#)). The RF model is a black box and is totally
800 reliant on the training dataset, which may reduce its robustness and applicability under certain
801 conditions. For comparison, a simple multiple linear regression (MLR) method was also tested using
802 the SCOPE simulation, but the results (Figure S4 in the Supplementary materials) were much worse
803 than the RF model (as shown in Figure 7), which confirmed that the RF model was more efficient to
804 estimate the SIF escape probability based on the information from reflectance.

805 A physical analysis based on the spectral invariant theory was carried out to improve the
806 robustness of the SIF downscaling model and find out the most important variables. However, there
807 are some limitations remaining in using the spectral invariant theory. In the spectral invariant theory,
808 the leaf reflectance and transmittance are combined as the leaf single scattering albedo. In other
809 words, the different transfer processes of the photons scattered downwards and upwards by leaves
810 were ignored. [Yang and Van der Tol \(2018\)](#) analyzed the radiative transfer of incident light and
811 emitted SIF considering the leaf reflectance and transmittance separately and got the same equation
812 as Eq. (14). But they pointed out that the equation was not valid for the red band due to the difference
813 between the leaf reflectance and transmittance. At the far-red band, the influence of the difference of
814 leaf reflectance and transmittance becomes relatively small with the increasing interaction order. At
815 the red band, however, the difference of leaf reflectance and transmittance is not ignorable because
816 the single scattering dominates. Nevertheless, [Yang and Van der Tol \(2018\)](#) also found that the ε_{CL}
817 and $\frac{BRF}{i_0\omega_L}$ were still proportional at the red band for individual leaves, but the slope of the
818 relationship was influenced by the leaf structure and pigment composition. In our study, we did not
819 rely on the physical analysis for SIF downscaling, but only used the spectral invariant theory to find
820 out the key parameters to estimate the SIF escape probability. Therefore, the results of this study

821 were not directly influenced by the limitations of the spectral invariant theory, and the SIF
822 downscaling at the red band was still reasonable and valid, although the accuracy was lower than
823 that at the far-red band.

824 We used different data stemming from models, field and airborne observations to assess
825 reliability of our approach. Although we could demonstrate consistency of downscaling results across
826 levels and experiments, particularly results obtained from *HyPlant* data were less clear compared to
827 modeling results. This is expected and related to the wealth of factors determining real
828 measurements. Further, the atmospheric correction of airborne measured radiance data to retrieve
829 surface reflectance and eventually calculate vegetation products such as fAPAR is a highly complex
830 task. Particularly canopy structure can introduce uncertainties in estimated irradiance due to varying
831 fractions of diffuse and direct irradiance components, thus causing errors in retrieved vegetation
832 products (Damm et al 2015b).

833 Other assumptions applied might also limit the scope of our analysis. i) The training dataset was
834 simulated with the SCOPE model. SCOPE provides relatively reliable simulations of SIF at PS, leaf and
835 canopy levels, and has been widely used in studies dealing with SIF (Damm et al. 2015a, Verrelst et al.
836 2016). However, SCOPE is a 1-D model and its simulations may only be reliable for canopies with a
837 relatively simple structure, such as crops and grass, and not for more complicated canopies such as
838 forest. The clumping effect was also neglected in the physical analysis. The performance of the
839 proposed method for the cases across canopies still needs to be further tested. ii) The estimated SIF
840 at PS level is not possible to be directly validated for ground or airborne measurements. $APAR_{chl}$ or
841 $fAPAR_{green}$ were, therefore, used to indirectly evaluate the reliability of estimated SIF_{PS} . But the
842 measurements or estimates of $APAR_{chl}$ or $fAPAR_{green}$ also contain uncertainties. Moreover, the

843 influence of SIF yield was neglected. Therefore, the validation of our SIF downscaling must be
844 elaborated in future work.

845 **5. Conclusions**

846 Remote sensing based SIF measurements at canopy level are largely affected by re-absorption
847 and scattering within the leaves and canopies, so the downscaling of SIF from canopy level to PS level
848 is important to better understand the link between SIF and GPP. A practicable solution based on
849 physical analysis and RF regression for the estimation of SIF escape probability was proposed. The RF
850 regression model was trained using SCOPE simulations. The results were evaluated using SCOPE and
851 DART simulations, field experiments and *HyPlant* image. The results indicate that, for the far-red
852 band, the SIF escape probability is dominated by the canopy scattering, while for the red band, the
853 SIF escape probability is related to both canopy scattering and reabsorption within leaves. We
854 conclude that accurate knowledge and correction of SIF escape probability is essential to reduce
855 associated large uncertainty in the SIF-APAR relationship, and this is also expected to improve the
856 SIF-based GPP estimation. Our suggested approach is based on the spectral invariant theory and
857 relies on canopy directional reflectance at the red, red-edge and far-red bands to downscale canopy
858 SIF to leaf or photosystem level. Although we could successfully demonstrate the reliability of our
859 approach, we identified strong sensitivity of our results to data quality and assumptions in
860 underlying models. We suggest advancing reliability of reflectance data retrievals in requested
861 wavelength ranges and further assessing the impact of assumptions underlying our analysis.

862

863 **Acknowledgements**

864 The authors gratefully acknowledge the financial support provided by the National Key R&D Program
865 of China (2017YFA0603001) and the National Natural Science Foundation of China (41701396,
866 41671349). L.G. has been supported by the Emmy Noether Programme of the German Research
867 Foundation (GU 1276/1-1). Z.M. has been supported by the Australian Research Council Future
868 Fellowship project (FT160100477). X.L. has been supported by the Sino-German (CSC-DAAD)
869 Postdoc Scholarship Program for his work in Germany. Acquisition of the *HyPlant* images and data
870 processing was supported by the European Space Agency (ESA) in the frame of the HyFLEX campaign
871 (ESA contract no. 4000107143/12/NL/FF/If CCN3), the SFB/TR 32 “Patterns in
872 Soil-Vegetation-Atmosphere Systems: Monitoring, Modelling, and Data Assimilation”—subproject D2
873 (www.tr32.de), funded by the Deutsche Forschungsgemeinschaft (DFG) and the German Plant
874 Phenotyping Network (DPPN; Förderkennzeichen 031A053A/B/C) of the BMBF. Additional financial
875 support was provided by the Forschungszentrum Jülich GmbH supporting the development and
876 operation of *HyPlant*. The authors thank Dr. Christiaan Van der Tol for providing the SCOPE code, and
877 thank Prof. Anatoly Gitelson for providing helpful suggestions in relation to fAPAR estimation, and
878 Patrick Rademske for supports related to providing the *HyPlant* dataset. The authors also thank the
879 editor and anonymous reviewers for their detailed and constructive suggestions for improving the
880 manuscript.

881 **References**

882 Abdel-Rahman, E.M., Ahmed, F.B., & Ismail, R. (2013). Random forest regression and spectral band
883 selection for estimating sugarcane leaf nitrogen concentration using EO-1 Hyperion hyperspectral

884 data. *International Journal of Remote Sensing*, 34, 712-728

885 Ač, A., Malenovský, Z., Olejníčková, J., Gallé, A., Rascher, U., Mohammed, G. (2015). Meta-analysis assessing
886 potential of steady-state chlorophyll fluorescence for remote sensing detection of plant water,
887 temperature and nitrogen stress. *Remote Sensing of Environment*, 168, 420-436

888 Adams, W.W., Winter, K., Schreiber, U., & Schramel, P. (1990). Photosynthesis and chlorophyll fluorescence
889 characteristics in relationship to changes in pigment and element composition of leaves of *Platanus*
890 *occidentalis* L. during autumnal leaf senescence. *Plant Physiology*, 92, 1184-1190

891 Agati, G., Fusi, F., Mazzinghi, P., & Paola, M. L. D. (1993). A simple approach to the evaluation of the
892 reabsorption of chlorophyll fluorescence spectra in intact leaves. *Journal of Photochemistry &*
893 *Photobiology B Biology*, 17(2), 163-171. Alonso, L., Gomez-Chova, L., Vila-Frances, J., Amoros-Lopez, J.,
894 Guanter, L., Calpe, J., & Moreno, J. (2008). Improved Fraunhofer Line Discrimination method for
895 vegetation fluorescence quantification. *IEEE Geoscience and Remote Sensing Letters*, 5, 620-624

896 Agati, G., Cerovic, Z. G., & Moya, I. (2000). The Effect of Decreasing Temperature up to Chilling Values on the
897 in vivo F685/F735 Chlorophyll Fluorescence Ratio in *Phaseolus vulgaris* and *Pisum sativum*: The
898 Role of the Photosystem I Contribution to the 735 nm Fluorescence Band. *Photochemistry and*
899 *Photobiology*, 72(1), 75-84.

900 Berry, J.A., Frankenberg, C., Wennberg, P., Baker, I., Bowman, K.W., Castro-Contreas, S., Cendrero-Mateo, M.P.,
901 Damm, A., Drewry, D., & Ehlmann, B. (2012). New methods for measurement of photosynthesis from
902 space. *Geophysical Research Letters*, 38, L17706

903 Breiman, L. (2001). Random forests. *Machine Learning*, 45, 5-32

904 Burkart A., Schickling A., Pilar Cendrero Mateo M., Wrobel T., Rossini M., Cogliati S., Julitta T., & Rascher, U.
905 (2015). A method for uncertainty assessment of passive sun-induced chlorophyll fluorescence
906 retrieval by using an infrared reference light. *IEEE Sensors*, 15, 4603-4611.

907 Chen, J.M., & Black, T. (1992). Defining leaf area index for non-flat leaves. *Plant, Cell & Environment*, 15,
908 421-429

909 Clevers, J.G., & Gitelson, A.A. (2013). Remote estimation of crop and grass chlorophyll and nitrogen content
910 using red-edge bands on Sentinel-2 and-3. *International Journal of Applied Earth Observation and*
911 *Geoinformation*, 23, 344-351

912 Cogliati S., Rossini M. Julitta T., Meroni, M. Schickling A., Burkart A., Pinto F., Rascher U., & Colombo R.
913 (2015). Continuous and long-term measurements of reflectance and sun-induced chlorophyll
914 fluorescence by using novel automated field spectroscopy systems. *Remote Sensing of Environment*,
915 164, 270-281.

916 Colwell, J.E. (1974). Vegetation canopy reflectance. *Remote Sensing of Environment*, 3, 175-183

917 Coops, N.C., Hilker, T., Hall, F.G., Nichol, C.J., & Drolet, G.G. (2010). Estimation of light-use efficiency of
918 terrestrial ecosystems from space: a status report. *Bioscience*, 60, 788-797

919 Córdón, G. B., & Lagorio, M. G. (2006). Re-absorption of chlorophyll fluorescence in leaves revisited. a
920 comparison of correction models. *Photochemical & Photobiological Sciences Official Journal of the*
921 *European Photochemistry Association & the European Society for Photobiology*, 5(8), 735-740.

922 Damm, A., Erler, A., Hillen, W., Meroni, M., Schaepman, M.E., Verhoef, W., & Rascher, U. (2011). Modeling the
923 impact of spectral sensor configurations on the FLD retrieval accuracy of sun-induced chlorophyll
924 fluorescence. *Remote Sensing of Environment*, 115, 1882-1892

925 Damm, A., Guanter, L., Laurent, V.C.E., Schaepman, M.E., Schickling, A., & Rascher, U. (2014). FLD-based
926 retrieval of sun-induced chlorophyll fluorescence from medium spectral resolution airborne
927 spectroscopy data. *Remote Sensing of Environment*, 147, 256-266

928 Damm, A., Guanter, L., Paul-Limoges, E., Van der Tol, C., Hueni, A., Buchmann, N., Eugster, W., Ammann, C., &
929 Schaepman, M.E. (2015a). Far-red sun-induced chlorophyll fluorescence shows ecosystem-specific
930 relationships to gross primary production: An assessment based on observational and modeling
931 approaches. *Remote Sensing of Environment*, 166, 91-105

932 Damm, A., Guanter, L., Verhoef, W., Schläpfer, D., Garbari, S., & Schaepman, M.E. (2015b). Impact of varying
933 irradiance on vegetation indices and chlorophyll fluorescence derived from spectroscopy data.
934 *Remote Sensing of Environment*, 156, 202-215

935 Dash, J., & Curran, P. (2004). The MERIS terrestrial chlorophyll index. *International Journal of Remote*
936 *Sensing*, 25, 5403-5413

937 Daumard, F., Goulas, Y., Champagne, S., Fournier, A., Ounis, A., Oliosio, A., & Moya, I. (2012). Continuous
938 Monitoring of Canopy Level Sun-Induced Chlorophyll Fluorescence During the Growth of a Sorghum
939 Field. *IEEE Transactions on Geoscience and Remote Sensing*, PP, 1-9

940 Du, S., Liu, L., Liu, X., & Hu, J. (2017). Response of Canopy Solar-Induced Chlorophyll Fluorescence to the
941 Absorbed Photosynthetically Active Radiation Absorbed by Chlorophyll. *Remote Sensing*, 9, 911

942 Field, C.B., Behrenfeld, M.J., Randerson, J.T., & Falkowski, P. (1998). Primary production of the biosphere:
943 Integrating terrestrial and oceanic components. *Science*, 281, 237-240

944 Fournier, A., Daumard, F., Champagne, S., Ounis, A., Goulas, Y., & Moya, I. (2012). Effect of canopy structure
945 on sun-induced chlorophyll fluorescence. *ISPRS Journal of Photogrammetry and Remote Sensing*, 68,
946 112-120

947 Frankenberg, C., Fisher, J.B., Worden, J., Badgley, G., Saatchi, S.S., Lee, J.-E., Toon, G.C., Butz, A., Jung, M., Kuze,
948 A., & Yokota, T. (2011). New global observations of the terrestrial carbon cycle from GOSAT: Patterns
949 of plant fluorescence with gross primary productivity. *Geophysical Research Letters*, 38

950 Gastellu-Etchegorry, J.-P., Lauret, N., Yin, T., Landier, L., Kallel, A., Malenovsky, Z., Al Bitar, A., Aval, J.,
951 Benhmida, S., & Qi, J. (2017). DART: Recent Advances in Remote Sensing Data Modeling With
952 Atmosphere, Polarization, and Chlorophyll Fluorescence. *IEEE Journal of Selected Topics in Applied*
953 *Earth Observations and Remote Sensing*

954 Gastellu-Etchegorry, J.-P., Yin, T., Lauret, N., Cajgfinger, T., Gregoire, T., Grau, E., Feret, J.-B., Lopes, M.,
955 Guilleux, J., & Dedieu, G. (2015). Discrete Anisotropic Radiative Transfer (DART 5) for modeling
956 airborne and satellite spectroradiometer and LIDAR acquisitions of natural and urban landscapes.
957 *Remote Sensing*, 7, 1667-1701

958 Gitelson, A.A., Buschmann, C., & Lichtenthaler, H.K. (1998). Leaf chlorophyll fluorescence corrected for
959 re-absorption by means of absorption and reflectance measurements. *Journal of Plant Physiology*,
960 152, 283-296

961 Gitelson, A.A., Peng, Y., & Huemmrich, K.F. (2014). Relationship between fraction of radiation absorbed by
962 photosynthesizing maize and soybean canopies and NDVI from remotely sensed data taken at close
963 range and from MODIS 250m resolution data. *Remote Sensing of Environment*, 147, 108-120

964 Gitelson, A.A., Vina, A., Ciganda, V., Rundquist, D.C., & Arkebauer, T.J. (2005). Remote estimation of canopy
965 chlorophyll content in crops. *Geophysical Research Letters*, 32

966 Goulas, Y., Fournier, A., Daumard, F., Champagne, S., Ounis, A., Marloie, O., & Moya, I. (2017). Gross Primary
967 Production of a Wheat Canopy Relates Stronger to Far Red Than to Red Solar-Induced Chlorophyll
968 Fluorescence. *Remote Sensing*, 9, 97

969 Green, J.K., Konings, A.G., Alemohammad, S.H., Berry, J., Entekhabi, D., Kolassa, J., Lee, J.E., & Gentine, P.
970 (2017). Regionally strong feedbacks between the atmosphere and terrestrial biosphere. *Nature*
971 *Geoscience*, 10, 410-414

- 972 Grossmann, K. (2014). PhotoSpec-Ground-based Remote Sensing of Solar-Induced Chlorophyll
973 Fluorescence. *Journal of Experimental Botany*, 22, 095
- 974 Guanter, L., Frankenberg, C., Dudhia, A., Lewis, P. E., Gómez-Dans, J., Kuze, A., ... & Grainger, R. G. (2012).
975 Retrieval and global assessment of terrestrial chlorophyll fluorescence from GOSAT space
976 measurements. *Remote Sensing of Environment*, 121, 236-251
- 977 Guanter, L., Zhang, Y., Jung, M., Joiner, J., Voigt, M., Berry, J.A., Frankenberg, C., Huete, A.R., Zarco-Tejada, P., &
978 Lee, J.-E. (2014). Global and time-resolved monitoring of crop photosynthesis with chlorophyll
979 fluorescence. *Proceedings of the National Academy of Sciences*, 201320008
- 980 He, L., Chen, J.M., Liu, J., Mo, G., & Joiner, J. (2017). Angular Normalization of GOME-2 Sun-induced
981 Chlorophyll Fluorescence Observation as a Better Proxy of Vegetation Productivity. *Geophysical
982 Research Letters*, 44(11), 5691-5699.
- 983 Huang, D., Knyazikhin, Y., Dickinson, R.E., Rautiainen, M., Stenberg, P., Disney, M., Lewis, P., Cescatti, A., Tian,
984 Y., & Verhoef, W. (2007). Canopy spectral invariants for remote sensing and model applications.
985 *Remote Sensing of Environment*, 106, 106-122
- 986 Jacquemoud, S., & Baret, F. (1990). PROSPECT: A model of leaf optical properties spectra. *Remote Sensing
987 of Environment*, 34, 75-91
- 988 Jiang, D., Wang, N., Yang, X., & Liu, H. (2002). Dynamic properties of absorbed photosynthetic active
989 eadiation and its relation to crop yield [J]. *System Sciences and Comprehensive Studies In Agriculture*,
990 18. 51-54.
- 991 Joiner, J., Yoshida, Y., Vasilkov, A. P., Middleton, E. M., Campbell, P. K. E., & Kuze, A. (2012). Filling-in of
992 near-infrared solar lines by terrestrial fluorescence and other geophysical effects: simulations and
993 space-based observations from SCIAMACHY and GOSAT. *Atmospheric Measurement Techniques*, 5,
994 809-829
- 995 Joiner, J., Guanter, L., Lindstrot, R., Voigt, M., Vasilkov, A.P., Middleton, E.M., Huemmrich, K.F., Yoshida, Y., &
996 Frankenberg, C. (2013). Global monitoring of terrestrial chlorophyll fluorescence from moderate
997 spectral resolution near-infrared satellite measurements: methodology, simulations, and
998 application to GOME-2. *Atmospheric Measurement Techniques*, 6, 2803-2823
- 999 Joiner, J., Yoshida, Y., Vasilkov, A.P., Corp, L.A., & Middleton, E.M. (2011). First observations of global and
1000 seasonal terrestrial chlorophyll fluorescence from space. *Biogeosciences*, 8, 637-651
- 1001 Jordan, C.F. (1969). Derivation of leaf-area index from quality of light on the forest floor. *Ecology*, 50,
1002 663-666
- 1003 Köhler, P., Guanter, L., & Joiner, J. (2015). A linear method for the retrieval of sun-induced chlorophyll
1004 fluorescence from GOME-2 and SCIAMACHY data. *Atmospheric Measurement Techniques*, 8,
1005 2589-2608
- 1006 Knyazikhin, Y., Kranigk, J., Myneni, R.B., Panfyorov, O., & Gravenhorst, G. (1998). Influence of small-scale
1007 structure on radiative transfer and photosynthesis in vegetation canopies. *Journal of Geophysical
1008 Research: Atmospheres*, 103, 6133-6144
- 1009 Knyazikhin, Y., Schull, M. A., Xu, L., Myneni, R. B., & Samanta, A. (2011). Canopy spectral invariants. Part 1: A
1010 new concept in remote sensing of vegetation. *Journal of Quantitative Spectroscopy and Radiative
1011 Transfer*, 112(4), 727-735.
- 1012 Knyazikhin, Y., Schull, M.A., Stenberg, P., Möttus, M., Rautiainen, M., Yang, Y., Marshak, A., Carmona, P.L.,
1013 Kaufmann, R.K., & Lewis, P. (2013). Hyperspectral remote sensing of foliar nitrogen content.
1014 *Proceedings of the National Academy of Sciences*, 110, E185-E192
- 1015 Liu, L., Guan, L., & Liu, X. (2017a). Directly estimating diurnal changes in GPP for C3 and C4 crops using

1016 far-red sun-induced chlorophyll fluorescence. *Agricultural and Forest Meteorology*, 232, 1-9

1017 Liu, L., Liu, X., & Hu, J. (2015). Effects of spectral resolution and SNR on the vegetation solar-induced

1018 fluorescence retrieval using FLD-based methods at canopy level. *European Journal of Remote*

1019 *Sensing*, 48, 743-762

1020 Liu, L., Liu, X., Hu, J., & Guan, L. (2017b). Assessing the wavelength-dependent ability of solar-induced

1021 chlorophyll fluorescence to estimate the GPP of winter wheat at the canopy level. *International*

1022 *Journal of Remote Sensing*, 38, 4396-4417

1023 Liu, L., Liu, X., Wang, Z., & Zhang, B. (2016). Measurement and Analysis of Bidirectional SIF Emissions in

1024 Wheat Canopies. *IEEE Transactions on Geoscience and Remote Sensing*, 54, 2640-2651

1025 Liu, L., Peng, D., Hu, Y., & Jiao, Q. (2013). A novel in situ FPAR measurement method for low canopy

1026 vegetation based on a digital camera and reference panel. *Remote Sensing*, 5, 274-281

1027 Liu, L.Y., Zhang, Y.J., Wang, J.H., & Zhao, C.J. (2005). Detecting solar-induced chlorophyll fluorescence from

1028 field radiance spectra based on the Fraunhofer line principle. *IEEE Transactions on Geoscience and*

1029 *Remote Sensing*, 43, 827-832

1030 Liu, X., Liu, L., Zhang, S., & Zhou, X. (2015). New spectral fitting method for full-spectrum solar-induced

1031 chlorophyll fluorescence retrieval based on principal components analysis. *Remote Sensing*, 7(8),

1032 10626-10645.

1033 Ma, C., Zhang, H. H., & Wang, X. (2014). Machine learning for Big Data analytics in plants. *Trends in plant*

1034 *science*, 19(12), 798-808.

1035 Maier, S.W., Günther, K.P., & Stellmes, M. (2003). Sun-induced fluorescence: A new tool for precision

1036 farming. In M. McDonald, J. Schepers, L. Tartly, T.v. Toai, & D. Major (Eds.), *Digital imaging and*

1037 *spectral techniques: Applications to precision agriculture and crop physiology* (pp. 209-222). Madison,

1038 WI, USA: American Society of Agronomy Special Publication

1039 Malenovský, Z., Mishra, K.B., Zemek, F., Rascher, U., Nedbal, L. (2009). Scientific and technical challenges in

1040 remote sensing of plant canopy reflectance and fluorescence. *Journal of Experimental Botany*, 60(11),

1041 2987-3004

1042 Malenovský, Z., Homolová, L., Zurita-Milla, R., Lukeš, P., Kaplan, V., Hanuš, J., Gastellu-Etchegorry, J-P,

1043 Schaepman, M.E. (2013). Retrieval of spruce leaf chlorophyll content from airborne image data

1044 using continuum removal and radiative transfer. *Remote Sensing of Environment*, 131, 85-102.

1045 Meroni, M., Busetto, L., Colombo, R., Guanter, L., Moreno, J., & Verhoef, W. (2010). Performance of Spectral

1046 Fitting Methods for vegetation fluorescence quantification. *Remote Sensing of Environment*, 114,

1047 363-374

1048 Migliavacca, M., Perez-Priego, O., Rossini, M., El-Madany, T.S., Moreno, G., Van der Tol, C., Rascher, U.,

1049 Berninger, A., Bessenbacher, V., & Burkart, A. (2017). Plant functional traits and canopy structure

1050 control the relationship between photosynthetic CO₂ uptake and far-red sun-induced fluorescence

1051 in a Mediterranean grassland under different nutrient availability. *New Phytologist*, 214, 1078-1091

1052 Monteith, J. (1972). Solar radiation and productivity in tropical ecosystems. *Journal of Applied Ecology*, 9(3),

1053 747-766

1054 Monteith, J.L., & Moss, C. (1977). Climate and the efficiency of crop production in Britain. *Philosophical*

1055 *Transactions of the Royal Society of London. Series B, Biological Sciences*, 281(980), 277-294

1056 Moya, I., & Cerovic, Z.G. (2004). Remote sensing of chlorophyll fluorescence: instrumentation and analysis.

1057 In G.C. Papageorgiou, & Govindgee (Eds.), *Chlorophyll a Fluorescence* (pp. 429-445). Kluwer,

1058 Dordrecht: Springer

1059 Moya, I., Daumard, F., Moise, N., Ounis, A., & Goulas, Y. (2006). First airborne multiwavelength passive

1060 chlorophyll fluorescence measurements over La Mancha (Spain) fields. *Second Recent Advances in*
1061 *Quantitative Remote Sensing*, 820-825.

1062 Nilson, T. (1971). A theoretical analysis of the frequency of gaps in plant stands. *Agricultural Meteorology*, 8,
1063 25-38

1064 Pfündel, E. (1998). Estimating the contribution of photosystem I to total leaf chlorophyll
1065 fluorescence. *Photosynthesis Research*, 56(2), 185-195.

1066 Pinto, F., Müller-Linow, M., Schickling, A., Cendrero-Mateo, M. P., Ballvora, A., & Rascher, U. (2017).
1067 Multiangular Observation of Canopy Sun-Induced Chlorophyll Fluorescence by Combining Imaging
1068 Spectroscopy and Stereoscopy. *Remote Sensing*, 9(5), 415.

1069 Plascyk, J.A. (1975). The MK II Fraunhofer line discriminator (FLD-II) for airborne and orbital remote
1070 sensing of solar-stimulated luminescence. *Optical Engineering*, 14, 339-346

1071 Porcar-Castell, A., Tyystjärvi, E., Atherton, J., Van der Tol, C., Flexas, J., Pfündel, E.E., Moreno, J., Frankenberg,
1072 C., & Berry, J.A. (2014). Linking chlorophyll a fluorescence to photosynthesis for remote sensing
1073 applications: mechanisms and challenges. *Journal of Experimental Botany*, eru191

1074 Ramos, M.E., & Lagorio, M.G. (2004). True fluorescence spectra of leaves. *Photochem Photobiol Sci*, 3,
1075 1063-1066

1076 Rascher, U., Alonso, L., Burkart, A., Cilia, C., Cogliati, S., Colombo, R., Damm, A., Drusch, M., Guanter, L., &
1077 Hanus, J. (2015). Sun-induced fluorescence—a new probe of photosynthesis: First maps from the
1078 imaging spectrometer HyPlant. *Global Change Biology*, 21, 4673-4684

1079 Romero, J.M., Cordon, G.B., & Lagorio, M.G. (2018). Modeling re-absorption of fluorescence from the leaf to
1080 the canopy level. *Remote Sensing of Environment*, 204, 138-146

1081 Rouse, J., Haas, R., Schell, J., & Deering, D. (1973). Monitoring vegetation systems in the Great Plains with
1082 ERTS (Earth Resources Technology Satellite). In, *Proceedings of 3rd ERTS Symposium* (pp. 48-62)

1083 Ross, J. (2012). *The radiation regime and architecture of plant stands*. Springer Science & Business Media

1084 Ryu, Y., Sonnentag, O., Nilson, T., Vargas, R., Kobayashi, H., Wenk, R., & Baldocchi, D.D. (2010). How to
1085 quantify tree leaf area index in an open savanna ecosystem: a multi-instrument and multi-model
1086 approach. *Agricultural and Forest Meteorology*, 150, 63-76

1087 Sellers, P., Tucker, C., Collatz, G., Los, S., Justice, C., Dazlich, D., & Randall, D. (1994). A global 1 by 1 NDVI
1088 data set for climate studies. Part 2: The generation of global fields of terrestrial biophysical
1089 parameters from the NDVI. *International Journal of Remote Sensing*, 15, 3519-3545

1090 Sims, D.A., & Gamon, J.A. (2002). Relationships between leaf pigment content and spectral reflectance
1091 across a wide range of species, leaf structures and developmental stages. *Remote Sensing of*
1092 *Environment*, 81, 337-354

1093 Smolander, S., & Stenberg, P. (2005). Simple parameterizations of the radiation budget of uniform
1094 broadleaved and coniferous canopies. *Remote Sensing of Environment*, 94, 355-363

1095 Soudani, K., Hmimina, G., Delpierre, N., Pontailier, J.-Y., Aubinet, M., Bonal, D., Caquet, B., De Grandcourt, A.,
1096 Burban, B., & Flechard, C. (2012). Ground-based Network of NDVI measurements for tracking
1097 temporal dynamics of canopy structure and vegetation phenology in different biomes. *Remote*
1098 *Sensing of Environment*, 123, 234-245

1099 Stenberg, P., Möttus, M., & Rautiainen, M. (2016). Photon recollision probability in modelling the radiation
1100 regime of canopies — A review. *Remote Sensing of Environment*, 183, 98-108

1101 Sun, Y., Frankenberg, C., Wood, J.D., Schimel, D., Jung, M., Guanter, L., Drewry, D., Verma, M., Porcar-Castell,
1102 A., & Griffis, T.J. (2017). OCO-2 advances photosynthesis observation from space via solar-induced
1103 chlorophyll fluorescence. *Science*, 358, eaam5747

- 1104 Van der Tol, C., Verhoef, W., Timmermans, J., Verhoef, A., & Su, Z. (2009). An integrated model of soil-canopy
 1105 spectral radiances, photosynthesis, fluorescence, temperature and energy balance. *Biogeosciences*, 6,
 1106 3109-3129
- 1107 Van der Tol, C., Berry, J. A., Campbell, P. K. E., & Rascher, U. (2014). Models of fluorescence and
 1108 photosynthesis for interpreting measurements of solar-induced chlorophyll fluorescence. *Journal of*
 1109 *Geophysical Research: Biogeosciences*, 119(12), 2312-2327
- 1110 Van Wittenberghe, S., Alonso, L., Verrelst, J., Moreno, J., & Samson, R. (2015). Bidirectional sun-induced
 1111 chlorophyll fluorescence emission is influenced by leaf structure and light scattering properties —
 1112 A bottom-up approach. *Remote Sensing of Environment*, 158, 169-179
- 1113 Verhoef, W. (1984). Light scattering by leaf layers with application to canopy reflectance modeling: the
 1114 SAIL model. *Remote Sensing Of Environment*, 16(2), 125-141
- 1115 Verrelst, J., Rivera, J.P., Van der Tol, C., Magnani, F., Mohammed, G., & Moreno, J. (2015). Global sensitivity
 1116 analysis of the SCOPE model: What drives simulated canopy-leaving sun-induced fluorescence.
 1117 *Remote Sensing of Environment*, 166, 8-2
- 1118 Vilfan, N., Van der Tol, C., Muller, O., Rascher, U., & Verhoef, W. (2016). Fluspect-B: A model for leaf
 1119 fluorescence, reflectance and transmittance spectra. *Remote Sensing of Environment*, 186, 596-615
- 1120 Viña, A., & Gitelson, A.A. (2005). New developments in the remote estimation of the fraction of absorbed
 1121 photosynthetically active radiation in crops. *Geophysical Research Letters*, 32Wang, Y., Buermann, W.,
 1122 Stenberg, P., Smolander, H., Häme, T., Tian, Y., Hu, J., Knyazikhin, Y., & Myneni, R.B. (2003). A new
 1123 parameterization of canopy spectral response to incident solar radiation: Case study with
 1124 hyperspectral data from pine dominant forest. *Remote Sensing of Environment*, 85, 304-315
- 1125 Wieneke, S., Ahrends, H., Damm, A., Pinto, F., Stadler, A., Rossini, M., & Rascher, U. (2016). Airborne based
 1126 spectroscopy of red and far-red sun-induced chlorophyll fluorescence: Implications for improved
 1127 estimates of gross primary productivity. *Remote Sensing of Environment*, 184, 654-667
- 1128 Wyber, R., Malenovský, Z., Ashcroft, M.B., Osmond, B., Robinson, S.A. (2017). Do Daily and Seasonal Trends
 1129 in Leaf Solar Induced Fluorescence Reflect Changes in Photosynthesis, Growth or Light Exposure?
 1130 *Remote Sensing*, 9(6), 604
- 1131 Xiao, X., Zhang, Q., Braswell, B., Urbanski, S., Boles, S., Wofsy, S., Moore, B., & Ojima, D. (2004). Modeling
 1132 gross primary production of temperate deciduous broadleaf forest using satellite images and
 1133 climate data. *Remote Sensing of Environment*, 91, 256-270
- 1134 Yan, G., Ren, H., Hu, R., Yan, K., & Zhang, W. (2012). A portable Multi-Angle Observation System. In,
 1135 *Geoscience and Remote Sensing Symposium (IGARSS), 2012 IEEE International* (pp. 6916-6919): IEEE
- 1136 Yang, P., & Van der Tol, C. (2018). Linking canopy scattering of far-red sun-induced chlorophyll
 1137 fluorescence with reflectance. *Remote Sensing Of Environment*, 209, 456-467
- 1138 Yang, X., Tang, J., Mustard, J.F., Lee, J.-E., Rossini, M., Joiner, J., Munger, J.W., Kornfeld, A., & Richardson, A.D.
 1139 (2015). Solar-induced chlorophyll fluorescence correlates with canopy photosynthesis on diurnal
 1140 and seasonal scales in a temperate deciduous forest. *Geophysical Research Letters*, 2015GL063201
- 1141 Zarco-Tejada, P.J., Catalina, A., González, M.R., & Martín, P. (2013). Relationships between net
 1142 photosynthesis and steady-state chlorophyll fluorescence retrieved from airborne hyperspectral
 1143 imagery. *Remote Sensing of Environment*, 136, 247-258
- 1144 Zhang, Y., Guanter, L., Berry, J.A., Van der Tol, C., Yang, X., Tang, J., & Zhang, F. (2016). Model-based analysis
 1145 of the relationship between sun-induced chlorophyll fluorescence and gross primary production for
 1146 remote sensing applications. *Remote Sensing of Environment*, 187, 145-155